

Higher-Rank Irreducible Cartesian Tensors for Equivariant Message Passing

Viktor Zaverkin¹ Francesco Alesiani¹ Takashi Maruyama¹ Federico Errica¹
 Henrik Christiansen¹ Makoto Takamoto¹ Nicolas Weber¹ Mathias Niepert^{1,2}

¹NEC Laboratories Europe ²University of Stuttgart
 viktor.zaverkin@neclab.eu

Abstract

The ability to perform fast and accurate atomistic simulations is crucial for advancing the chemical sciences. By learning from high-quality data, machine-learned interatomic potentials achieve accuracy on par with ab initio and first-principles methods at a fraction of their computational cost. The success of machine-learned interatomic potentials arises from integrating inductive biases such as equivariance to group actions on an atomic system, e.g., equivariance to rotations and reflections. In particular, the field has notably advanced with the emergence of equivariant message-passing architectures. Most of these models represent an atomic system using spherical tensors, tensor products of which require complicated numerical coefficients and can be computationally demanding. This work introduces higher-rank irreducible Cartesian tensors as an alternative to spherical tensors, addressing the above limitations. We integrate irreducible Cartesian tensor products into message-passing neural networks and prove the equivariance of the resulting layers. Through empirical evaluations on various benchmark data sets, we consistently observe on-par or better performance than that of state-of-the-art spherical models.

1 Introduction

The ability to perform sufficiently fast and accurate atomistic simulations for large molecular and material systems holds the potential to revolutionize molecular and materials science [1–8]. Conventionally, computational chemistry and materials science rely on ab initio or first-principles approaches—e.g., coupled cluster [9–11] or density functional theory (DFT) [12, 13], respectively—that are accurate but computationally demanding, thus limiting the accessible simulation time and system sizes. However, the ability to generate high-quality, first-principles-based data sets has prompted the development of machine-learned interatomic potentials (MLIPs). These potentials enable atomistic simulations with accuracy that is on par with the reference first-principles method but at a fraction of the computational cost. Message-passing neural networks (MPNNs) [14–21] have been employed in chemical and materials sciences, including the development of MLIPs, due to their efficient processing of the graph representation of the atomic system [22–26]. Achieving the desired MLIPs’ performance, however, requires the inclusion of inductive biases, like the invariance of total energy to translations, reflections, and rotations in the three-dimensional space, and an effective encoding of the atomic system into a learnable representation [27]. Designing equivariant MPNNs [25, 26, 28–36], which preserve the directional information of the local atomic environment, has been one of the most active research directions of the last years. Previous work often achieves equivariance by representing an atomic system as a graph where node features are expressed in spherical harmonics basis and designing ad-hoc message-passing layers [25, 32–36].

MLIPs based on spherical harmonics [25, 33, 34], which are the basis for irreducible representations of the three-dimensional rotation group, often demonstrate a better performance compared to those

that use lower-rank Cartesian representations (scalars and vectors) [28, 37]. Spherical tensors, however, require the definition of a particular rotational axis, often chosen as the z -axis, resulting in inherent bias [38]. Furthermore, coupling spherical tensors via tensor products, involved in designing equivariant convolutions and constructing many-body features [33, 39, 40], requires the definition of complicated numerical coefficients, e.g., Wigner 3- j symbols defined in terms of the Clebsch–Gordan coefficients [41], and can be computationally demanding. In contrast, irreducible Cartesian tensors have no preferential directions; their tensor products are simpler and have a better computational complexity—up to a certain tensor rank—than the tensor products of spherical tensors [38, 42–45]. Recent work [30] improved results of Cartesian MPNNs by decomposing rank-two tensors into irreducible representations of the three-dimensional rotation group, i.e., into representations of dimension 1 (trace), 3 (anti-symmetric part), and 5 (traceless symmetric part) [46].

Contributions. In this work, we demonstrate that operating with irreducible Cartesian tensors leads to on-par or, sometimes, even better performance than that of spherical counterparts. Particularly, this work goes beyond scalars, vectors, and rank-two tensors and explores the integration of higher-rank irreducible Cartesian tensors and their products into equivariant MPNNs: i) We demonstrate how irreducible Cartesian tensors that are symmetric and traceless can be constructed from a unit vector and a product of two irreducible Cartesian tensors; ii) We prove that the resulting tensors are equivariant under the action of the three-dimensional rotation and reflection group; iii) We demonstrate that higher-rank irreducible Cartesian tensors can be used to design cost-efficient—up a certain tensor rank—and accurate equivariant models of many-body interactions; iv) We conduct different experiments to assess the effectiveness of equivariant message passing based on irreducible Cartesian tensors, and achieve state-of-the-art performance on benchmark data sets such as rMD17 [47], 3BPA [48], and acetylacetone [32]. We hope our contributions will offer new insights into the use of Cartesian tensors for constructing accurate and cost-efficient MLIPs and beyond.

2 Background

Group representations and equivariance. A group (G, \cdot) is defined by a set of elements G and a group product \cdot . A representation D of a group is a function from G to square matrices such that $D[g]D[g'] = D[g \cdot g']$, $\forall g, g' \in G$. This representation defines an action of G to any vector space \mathcal{X} (of the same dimension as the dimension of square matrices) through the matrix-vector multiplication, i.e., $(g, \mathbf{x}) \mapsto D_{\mathcal{X}}[g]\mathbf{x}$ for $\forall g \in G$ and $\forall \mathbf{x} \in \mathcal{X}$. For vector spaces \mathcal{X} and \mathcal{Y} , a function $f : \mathcal{X} \rightarrow \mathcal{Y}$ is called equivariant to the action of a group G to \mathcal{X} and \mathcal{Y} iff

$$f(D_{\mathcal{X}}[g]\mathbf{x}) = D_{\mathcal{Y}}[g]f(\mathbf{x}), \forall g \in G.$$

Invariance can be seen as a special type of equivariance with $D_{\mathcal{Y}}[g]$ being the identity for all g . An important class of equivariant models focuses on equivariance to the action of the Euclidean group $E(3)$, comprising translations and the orthogonal group $O(3)$, i.e., rotation group $SO(3)$ and reflections, in \mathbb{R}^3 . MLIPs based on equivariant models usually focus on equivariance to the action of the orthogonal group $O(3)$ and are invariant to translations.

Cartesian tensors. A vector $\mathbf{x} \in \mathbb{R}^3$ transforms under the action of the rotation group $SO(3)$ as $\mathbf{x}' = R\mathbf{x}$, i.e., each component of it transforms as $(\mathbf{x}')_i = \sum_j R_{ij}(\mathbf{x})_j$. Here, $R = D_{\mathcal{X}}[g] \in \mathbb{R}^{3 \times 3}$ denotes the rotation matrix representation of $g \in SO(3)$. Cartesian tensors of rank n are described by 3^n numbers and generalize the concept of vectors. A rank- n Cartesian tensor \mathbf{T} can be viewed as a multidimensional array with n indices, i.e., $(\mathbf{T})_{i_1 i_2 \dots i_n}$ with $i_k \in \{1, 2, 3\}$ for $\forall k \in \{1, \dots, n\}$. Furthermore, each index of $(\mathbf{T})_{i_1 i_2 \dots i_n}$ transforms independently as a vector under rotation. For example, a rank-two tensor transforms under rotation as $\mathbf{T}' = R\mathbf{T}R^\top$, i.e., each component of it transforms as $(\mathbf{T}')_{i_1 i_2} = \sum_{j_1 j_2} R_{i_1 j_1} R_{i_2 j_2} (\mathbf{T})_{j_1 j_2}$. For Cartesian tensors, one defines an r -fold tensor contraction and an outer product, i.e., $(\mathbf{T})_{j_1 \dots j_s} = \sum_{i_1, \dots, i_r} (\mathbf{U})_{i_1 \dots i_r j_1 \dots j_s} (\mathbf{S})_{i_1 \dots i_r}$ and $(\mathbf{T})_{i_1 \dots i_r j_1 \dots j_s} = (\mathbf{U})_{i_1 \dots i_r} (\mathbf{S})_{j_1 \dots j_s}$, respectively. Cartesian tensors are generally reducible and can, thus, be decomposed into smaller representations that transform independently within their linear subspaces under rotation. For example, a rank-two reducible Cartesian tensor contains representations of dimension 1 (trace), 3 (anti-symmetric part), and 5 (traceless symmetric part): $\sum_{i_1} (\mathbf{T})_{i_1 i_1}$, $(\mathbf{T})_{i_1 i_2} - (\mathbf{T})_{i_2 i_1}$, and $(\mathbf{T})_{i_1 i_2} + (\mathbf{T})_{i_2 i_1} - 2/3 \sum_{i_1} (\mathbf{T})_{i_1 i_1}$, respectively. Under rotation, the symmetric traceless part remains within its irreducible subspace, with a similar behavior for other irreducible components of $(\mathbf{T})_{i_1 i_2}$. Furthermore, for a reducible Cartesian tensor of rank n , an action

of the rotation group $\text{SO}(3)$ can be represented with a $3^n \times 3^n$ -dimensional rotation matrix. This rotation matrix is also reducible, meaning that an appropriate change of basis can block diagonalize it into smaller subsets, the irreducible representations of the rotation group $\text{SO}(3)$.

Spherical tensors. Spherical harmonics (or spherical tensors) Y_m^l are functions from the points on a sphere to complex or real numbers, with degree $l \geq 0$ and components $-l \leq m \leq l$. Collecting all components for a given l we obtain a $(2l + 1)$ -dimensional object $\mathbf{Y}^l = (Y_{-l}^l, \dots, Y_{l-1}^l, Y_l^l)$. Spherical tensors transform under rotation as $Y_m^l(R\hat{\mathbf{x}}) = \sum_{m'} (\mathbf{D})_{mm'}^l Y_{m'}^l(\hat{\mathbf{x}})$, where $(\mathbf{D})_{mm'}^l$ is the irreducible representation of $\text{SO}(3)$ —the Wigner D -matrix—and R denotes the rotation matrix. Spherical tensors are irreducible and can be combined using the Clebsch–Gordan tensor product

$$(Y_{m_1}^{l_1} \otimes_{\text{CG}} Y_{m_2}^{l_2})_{m_3}^{l_3} = \sum_{m_1=-l_1}^{l_1} \sum_{m_2=-l_2}^{l_2} C_{l_1 m_1, l_2 m_2}^{l_3 m_3} Y_{m_1}^{l_1} Y_{m_2}^{l_2},$$

with Clebsch–Gordan coefficients $C_{l_1 m_1, l_2 m_2}^{l_3 m_3}$ and $l_3 \in \{|l_1 - l_2|, \dots, l_1 + l_2\}$. Furthermore, any reducible Cartesian tensor of rank n can be written in spherical harmonics as $(\hat{\mathbf{x}})_{i_1} (\hat{\mathbf{x}})_{i_2} \dots (\hat{\mathbf{x}})_{i_n} = \sum_{l=0}^n \sum_{m=-l}^l X_{i_1 i_2 \dots i_n}^{lm} Y_m^l$, with coefficients $X_{i_1 i_2 \dots i_n}^{lm}$ defined elsewhere [49].

3 Related work

Higher-body-order local descriptors. Recent advances in MLIPs have been influenced by moment tensor potentials (MTP) [50] and atomic cluster expansion (ACE) [40]. These approaches enable systematic construction of higher-body-order polynomial basis functions, encompassing representations like atom-centered symmetry functions (ACSFs) [51, 52], smooth overlap of atomic positions (SOAP) [53, 54], Gaussian moments [55, 56], and embedded atom/multi-scale embedded atom method (EAM/MEAM) potentials [57, 58]. Furthermore, a reducible Cartesian tensor can be represented as a linear combination of irreducible spherical counterparts, and vice versa [40, 49]. More general expressions, including tensor contractions, have also been provided, hinting at the relationship between Cartesian and spherical models [59–61]. Despite the success of MTP and ACE, defining smaller cutoff radii and rigid architecture can result in limited accuracy compared to MPNNs.

Equivariant message-passing potentials. Equivariant MPNNs [25, 28–37, 39, 62–64] often outperform more traditional invariant counterparts [65–70]. While many invariant and equivariant MPNNs rely on two-body features within a single message-passing layer, there is a growing interest in incorporating higher-body-order features, such as angles and dihedrals, to model many-body interactions in atomic systems [67, 69, 70]. Note that equivariant models with two-body features in a single message-passing layer build many-body ones through numerous message-passing iterations, increasing the receptive field and, thus, computational cost. Refs. 67, 69 recognized the importance of higher-body-order features but faced challenges due to explicit summation over triplets or quadruplets. In contrast, MACE advances the current state-of-the-art by combining ACE and equivariant message passing, introducing cost-efficient many-body message-passing potentials [33]. With just two message-passing layers, MACE yields accurate potentials for interacting many-body systems [71].

Beyond Clebsch–Gordan tensor product. Despite the success of equivariant MPNNs based on spherical tensors, the high computational cost of the Clebsch–Gordan tensor product limits their computational efficiency [28, 30, 33–35, 63, 64, 72–74]. Thus, current research focuses on alternatives to the Clebsch–Gordan tensor product, which has a $\mathcal{O}(L^6)$ complexity for tensors up to degree L . Recently, the relation of Clebsch–Gordan coefficients to the integral of products of three spherical harmonics, known as the Gaunt coefficients [41], has been exploited to reduce the computational cost of the tensor product of spherical tensors to $\mathcal{O}(L^3)$ [36]. Alternatively, Cartesian tensors and their products can be used to construct message-passing layers with two- and many-body features. Recently, a competitive performance to spherical models for a Cartesian message-passing architecture based on decomposing rank-two tensors into their irreducible representations has been demonstrated [30]. In this case, all operations are performed on tensors or their decomposition, which has advantageous computational complexity compared to the Clebsch–Gordan tensor product. Furthermore, recent work employs higher-rank reducible Cartesian tensors to design many-body message-passing potentials but does not achieve the state-of-the-art performance of spherical counterparts [31]. This performance gap may result from mixing different irreducible representations during message-passing based on reducible Cartesian tensors and their products.

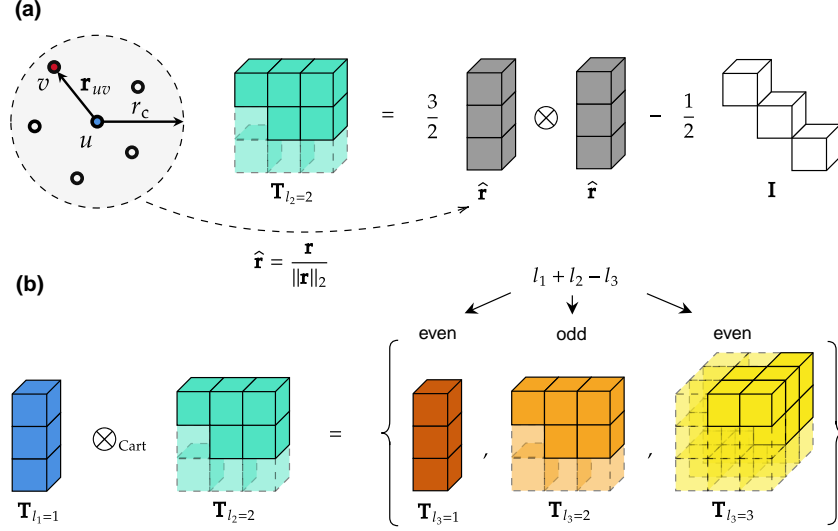


Figure 1: **Schematic illustration of (a) the construction of an irreducible Cartesian tensor for a local atomic environment and (b) the tensor product of two irreducible Cartesian tensors of rank l_1 and l_2 .** The construction of an irreducible Cartesian tensor from a unit vector $\hat{\mathbf{r}}$ is defined in Eq. (1). In this work, we use tensors with the same rank n and weight l , i.e., $n = l$, avoiding the need for embedding tensors with $l < n$ in a higher-dimensional tensor space. Therefore, we use l to identify the rank and the weight of an irreducible Cartesian tensor throughout this work. The tensor product is defined in Eqs. (2) and (3), resulting in a new tensor $\mathbf{T}_{l_3} = (\mathbf{T}_{l_1} \otimes_{\text{Cart}} \mathbf{T}_{l_2})_{l_3}$ of rank $l_3 = \{|l_1 - l_2|, \dots, l_1 + l_2\}$. Transparent boxes denote the linearly dependent elements of symmetric and traceless tensors. The tensor product yields even and odd parity tensors \mathbf{T}_{l_3} , given by $l_1 + l_2 - l_3$.

4 Methods

We define an atomic configuration $\mathcal{S} = \{\mathbf{r}_u, Z_u\}_{u=1}^{N_{\text{at}}}$, where $\mathbf{r}_u \in \mathbb{R}^3$ denotes Cartesian coordinates and $Z_u \in \mathbb{N}$ represents the atomic number of atom u , with a total of N_{at} atoms. Our focus lies on message-passing MLIPs, parameterized by θ , that learn a mapping from a configuration \mathcal{S} to the total energy E , i.e., $f_\theta : \mathcal{S} \mapsto E \in \mathbb{R}$. Thus, we represent molecular and material systems as graphs in a three-dimensional Euclidean space. An edge $\{u, v\}$ exists if atoms u and v are within a cutoff distance r_c , i.e., $\|\mathbf{r}_u - \mathbf{r}_v\|_2 \leq r_c$. For more details on MPNNs, see Appendix A. The total energy of an atomic configuration is defined by the sum of individual atomic energy contributions [51], i.e., $E = \sum_{u=1}^{N_{\text{at}}} E_u$. Atomic forces are computed as negative gradients of the total energy with respect to atomic coordinates, i.e., $\mathbf{F}_u = -\nabla_{\mathbf{r}_u} E$.

4.1 Irreducible Cartesian tensor product

In the following, we explore irreducible Cartesian tensors and their products based on the three-dimensional vector space and the three-dimensional orthogonal group $O(3)$, which comprises rotations and reflections. The respective tensors and tensor products are schematically illustrated in Fig. 1 (a) and (b), respectively, and are further employed in constructing MPNNs for atomic systems equivariant under actions of the orthogonal group. An irreducible Cartesian tensor $\mathbf{T}_n \in (\mathbb{R}^3)^{\otimes n}$ of rank n and weight $l \leq n$ (related to the degree l of spherical tensors) can be represented by a tensor with 3^n components in a three-dimensional vector space. These 3^n components form a basis for a $(2l + 1)$ -dimensional irreducible representation of the three-dimensional rotation group $SO(3)$ [75, 76]. Thus, only $2l + 1$ of the 3^n components are independent.

The rotation in the space of all tensors of rank n is induced through the n -fold outer product of a rotation matrix $R \in \mathbb{R}^{3 \times 3}$, i.e., $R^{\otimes n} = R \otimes \dots \otimes R$. The obtained representation of the rotation group $SO(3)$ is reducible for all n except $n = \{0, 1\}$. Reducing a tensor of rank n yields a unique irreducible tensor with the same weight and rank ($n = l$), which is characterized by being symmetric, i.e., $(\mathbf{T}_n)_{\dots i \dots j \dots} = (\mathbf{T}_n)_{\dots j \dots i \dots}$, $\forall i \neq j \in \{i_1 \dots, i_n\}$, and traceless, i.e.,

$\sum_i (\mathbf{T}_n)_{\dots i \dots} = 0, \forall i \in \{i_1, \dots, i_n\}$. An irreducible tensor of rank n and weight l with $l < n$ can be viewed as a l -rank tensor embedded in the n -rank tensor space, e.g., by computing an outer product with the identity matrix. However, the embedding is often not unique. Thus, we construct tensors with the same weight and rank ($n = l$) in the following.

Irreducible Cartesian tensors from unit vectors. Hereafter, we denote the rank and the weight of irreducible Cartesian tensors by l to distinguish them from reducible counterparts. An irreducible Cartesian tensor of an arbitrary rank l can be constructed from a unit vector $\hat{\mathbf{r}}$ in the form [45]

$$\mathbf{T}_l(\hat{\mathbf{r}}) = C \sum_{m=0}^{\lfloor l/2 \rfloor} (-1)^m \frac{(2l - 2m - 1)!!}{(2l - 1)!!} \{ \hat{\mathbf{r}}^{\otimes(l-2m)} \otimes \mathbf{I}^{\otimes m} \}, \quad (1)$$

resulting in a symmetric and traceless tensor of rank l . Here, \mathbf{I} denotes the 3×3 identity matrix, $\hat{\mathbf{r}}^{\otimes(l-2m)} = \hat{\mathbf{r}} \otimes \dots \otimes \hat{\mathbf{r}}$ and $\mathbf{I}^{\otimes m} = \mathbf{I} \otimes \dots \otimes \mathbf{I}$ are the corresponding $(l - 2m)$ - and m -fold outer products. The curly brackets indicate the summation over all permutations of the l unsymmetrized indices [45], i.e., $\{ \mathbf{T}_l \}_{i_1 \dots i_l} = \sum_{\pi \in S_l} (\mathbf{T}_l)_{i_{\pi(1)} \dots i_{\pi(l)}}$, with S_l being the corresponding set of permutations. The expression in Eq. (1) involves three distinct outer products $(\hat{\mathbf{r}} \otimes \hat{\mathbf{r}})_{i_1 i_2} = \hat{r}_{i_1} \hat{r}_{i_2}$, $(\mathbf{I} \otimes \mathbf{I})_{i_1 i_2 i_3 i_4} = \delta_{i_1 i_2} \delta_{i_3 i_4}$, and $(\hat{\mathbf{r}} \otimes \mathbf{I})_{i_1 i_2 i_3} = \hat{r}_{i_1} \delta_{i_2 i_3}$, where $\delta_{i_2 i_3}$ denotes the Kronecker delta. The normalization constant $C = (2l - 1)!!/l!$ is chosen such that an l -fold contraction of \mathbf{T}_l with the unit vector $\hat{\mathbf{r}}$ yields unity. An example of an irreducible Cartesian tensor with rank $l = 3$ is $(\mathbf{T}_{l=3})_{i_1 i_2 i_3} = \frac{5}{2}(\hat{r}_{i_1} \hat{r}_{i_2} \hat{r}_{i_3} - \frac{1}{5}(\hat{r}_{i_1} \delta_{i_2 i_3} + \hat{r}_{i_2} \delta_{i_3 i_1} + \hat{r}_{i_3} \delta_{i_1 i_2}))$.

Irreducible Cartesian tensor product. The following defines the product of two irreducible Cartesian tensors $\mathbf{x}_{l_1} \in (\mathbb{R}^3)^{\otimes l_1}$ and $\mathbf{y}_{l_2} \in (\mathbb{R}^3)^{\otimes l_2}$, yielding an irreducible Cartesian tensor of rank l_3 , i.e., $\mathbf{z}_{l_3} = (\mathbf{x}_{l_1} \otimes_{\text{Cart}} \mathbf{y}_{l_2})_{l_3} \in (\mathbb{R}^3)^{\otimes l_3} \forall l_3 \in \{|l_1 - l_2|, \dots, l_1 + l_2\}$, that is symmetric and traceless. The irreducible Cartesian tensor product is crucial for designing equivariant MPNNs and is used for equivariant convolutions and constructing many-body features in Section 4.2. For an even $l_1 + l_2 - l_3 = 2k$, the general form of an irreducible Cartesian tensor of rank l_3 reads [45]

$$(\mathbf{x}_{l_1} \otimes_{\text{Cart}} \mathbf{y}_{l_2})_{l_3} = C_{l_1 l_2 l_3} \sum_{m=0}^{\min(l_1, l_2) - k} (-1)^m 2^m \frac{(2l_3 - 2m - 1)!!}{(2l_3 - 1)!!} \{ (\mathbf{x}_{l_1} \cdot (k + m) \cdot \mathbf{y}_{l_2}) \otimes \mathbf{I}^{\otimes m} \}, \quad (2)$$

where $(\mathbf{x}_{l_1} \cdot (k + m) \cdot \mathbf{y}_{l_2}) = \sum_{i_1, \dots, i_{k+m}} (\mathbf{x}_{l_1})_{i_1 \dots i_{k+m}} (\mathbf{y}_{l_2})_{i_1 \dots i_{k+m}}$ denotes an $(k + m)$ -fold tensor contraction, which results in a tensor of rank $l_1 + l_2 - 2(k + m)$. For simplicity, we skip the uncontracted indices in the above definition. For example, for $l_1 = 4$ and $l_2 = 3$ and a three-fold tensor contraction we obtain $(\mathbf{x}_{l_1} \cdot 3 \cdot \mathbf{y}_{l_2})_{i_4} = \sum_{i_1, i_2, i_3} (\mathbf{x}_{l_1})_{i_1 i_2 i_3 i_4} (\mathbf{y}_{l_2})_{i_1 i_2 i_3}$, i.e., the corresponding tensors are contracted along i_1, i_2 , and i_3 . Note that the final result is independent of the index permutation, as the contracted tensors are symmetric. For an odd $l_1 + l_2 - l_3 = 2k + 1$, we define [45]

$$(\mathbf{x}_{l_1} \otimes_{\text{Cart}} \mathbf{y}_{l_2})_{l_3} = D_{l_1 l_2 l_3} \sum_{m=0}^{\min(l_1, l_2) - k - 1} (-1)^m 2^m \frac{(2l_3 - 2m - 1)!!}{(2l_3 - 1)!!} \{ (\boldsymbol{\varepsilon} : \mathbf{x}_{l_1} \cdot (k + m) \cdot \mathbf{y}_{l_2}) \otimes \mathbf{I}^{\otimes m} \}, \quad (3)$$

with $\boldsymbol{\varepsilon}$ denoting the Levi-Civita symbol ($\varepsilon_{i_1 i_2 i_3} = -\varepsilon_{i_3 i_2 i_1}$ and $\varepsilon_{i_1 i_1 i_3} = 0$). The double contraction with the Levi-Civita symbol reads $(\boldsymbol{\varepsilon} : \mathbf{x}_{l_1} \cdot (k + m) \cdot \mathbf{y}_{l_2})_{i_1} = \sum_{i_2, i_3} \varepsilon_{i_1 i_2 i_3} (\mathbf{x}_{l_1} \cdot (k + m) \cdot \mathbf{y}_{l_2})_{i_2 i_3}$, and yields a tensor of rank $l_1 + l_2 - 2(k + m) - 1$. Details on the normalization constants $C_{l_1 l_2 l_3}$ and $D_{l_1 l_2 l_3}$ are provided in Appendix B.1.

4.2 Equivariant message-passing based on irreducible Cartesian tensors

The following section introduces the basic operations for constructing equivariant MPNNs based on irreducible Cartesian tensors. Using their irreducible tensor products, we also demonstrate how to build equivariant two- and many-body features, crucial for modeling many-body interactions in molecular and materials systems. Particularly, we focus on MLIPs based on equivariant MPNNs and extend the state-of-the-art MACE architecture [33] to the Cartesian basis. Following the MACE architecture, we use only tensors and tensor products of even parity. We split vectors $\mathbf{r}_{uv} = \mathbf{r}_u - \mathbf{r}_v \in \mathbb{R}^3$ from atom u to atom v , schematically shown in Fig. 1, into their radial and angular components (unit vectors), i.e., $r_{uv} = \|\mathbf{r}_{uv}\|_2 \in \mathbb{R}$ and $\hat{\mathbf{r}}_{uv} = \mathbf{r}_{uv}/r_{uv} \in \mathbb{R}^3$, respectively. In the t -th message-passing layer, edges $\{u, v\}$ are embedded using a fully connected neural network $R_{kl_1 l_2 l_3}^{(t)} : \mathbb{R} \rightarrow \mathbb{R}$

with k output feature channels. The radial function $R_{kl_1l_2l_3}^{(t)}$ takes as an input radial distances r_{uv} , which are embedded through Bessel functions and multiplied by a smooth polynomial function [70]. Finally, we use irreducible Cartesian tensors $\mathbf{T}_l(\hat{\mathbf{r}})$, similar to spherical tensors $\mathbf{Y}^l(\hat{\mathbf{r}})$, to embed unit vectors into the tensor space of maximal rank l_{\max} .

Equivariant convolutions and two-body features. Rotation equivariance in MPNNs is typically achieved by constraining convolution filters to be the products between learnable radial functions and spherical tensors, i.e., $R_{kl_1l_2l_3}^{(t)}(r_{uv})Y_{m_1}^{l_1}(\hat{\mathbf{r}}_{uv})$. The two-body features $A_{ukl_3m_3}^{(t)}$ are further obtained through the tensor product—the point-wise convolution [39]—between the respective filters and neighbors’ equivariant features $h_{ukl_2m_2}^{(t)}$. The permutational invariance is enforced by pooling over the neighbors $v \in \mathcal{N}(u)$. Here, we use irreducible Cartesian tensors, with the rotation-equivariant filters given by $R_{kl_1l_2l_3}^{(t)}(r_{uv})(\mathbf{T}_{l_1}(\hat{\mathbf{r}}_{uv}))_{i_1i_2\cdots i_{l_1}}$. Thus, two-body features $(\mathbf{A}_{ukl_3}^{(t)})_{i_1i_2\cdots i_{l_3}}$ are obtained using the irreducible Cartesian tensor product and are represented by rank- l_3 irreducible Cartesian tensors. The Cartesian two-body features are defined by

$$(\mathbf{A}_{ukl_3}^{(t)})_{i_1i_2\cdots i_{l_3}} = \sum_{v \in \mathcal{N}(u)} \left(R_{kl_1l_2l_3}^{(t)}(r_{uv}) \mathbf{T}_{l_1}(\hat{\mathbf{r}}_{uv}) \otimes_{\text{Cart}} \frac{1}{\sqrt{d_t}} \sum_{k'} W_{kk'l_2}^{(t)} \mathbf{h}_{vk'l_2}^{(t)} \right)_{i_1i_2\cdots i_{l_3}}, \quad (4)$$

where d_t represents the number of feature channels in the node embeddings $\mathbf{h}_{vk'l_2}^{(t)}$ of the t -th message-passing layer. In the first message-passing layer, node embeddings are initialized as learnable weights W_{kZ_v} that are invariant to actions of the orthogonal group, i.e., are scalars or tensors of rank $l_2 = 0$, and embed the atom type Z_v . Thus, constructing equivariant two-body features simplifies to

$$(\mathbf{A}_{ukl_1}^{(1)})_{i_1i_2\cdots i_{l_1}} = \sum_{v \in \mathcal{N}(u)} R_{kl_1}^{(1)}(r_{uv}) (\mathbf{T}_{l_1}(\hat{\mathbf{r}}_{uv}))_{i_1i_2\cdots i_{l_1}} W_{kZ_v}. \quad (5)$$

Equivariant many-body features. The importance of many-body terms arises from the fact that the interaction between atoms changes when additional atoms are present; see Appendix A. Furthermore, many-body terms are often required to ensure the transferability of interatomic potentials [77]. Here, we construct $(\nu + 1)$ -body equivariant features from $(\mathbf{A}_{ukl_\xi}^{(t)})_{i_1i_2\cdots i_{l_\xi}}$ obtained using Eqs. (4) or (5). The ν -fold Cartesian tensor product, which yields $(\nu + 1)$ -body features represented by an irreducible Cartesian tensor of rank L , reads

$$(\mathbf{B}_{u\eta_\nu kL}^{(t)})_{i_1i_2\cdots i_L} = \underbrace{(\tilde{\mathbf{A}}_{ukl_1}^{(t)} \otimes_{\text{Cart}} \cdots \otimes_{\text{Cart}} \tilde{\mathbf{A}}_{ukl_\nu}^{(t)})}_{\nu\text{-fold}}_{i_1i_2\cdots i_L}, \quad (6)$$

where η_ν counts all possible ν -fold products of $\{l_1, \dots, l_\nu\}$ -rank tensors, yielding rank- L irreducible Cartesian tensors, and $\tilde{\mathbf{A}}_{ukl_\xi}^{(t)} = \frac{1}{\sqrt{d_t}} \sum_{k'} W_{kk'l_\xi}^{(t)} \mathbf{A}_{uk'l_\xi}^{(t)}$ with d_t feature channels.

The irreducible Cartesian tensor product does not allow pre-computing the ν -fold tensor product, differing from spherical tensors that use the generalized Clebsch–Gordan coefficients for this purpose [33, 40, 49]. Thus, we obtain the result of Eq. (6) by successively computing ν -fold tensor products and refer to the respective models as irreducible Cartesian tensor potentials (ICTPs) with the full product basis or ICTP_{full}. However, the two-fold tensor product in Eq. (6) is symmetric to permutations of involved tensors. Thus, the number of the ν -fold tensor products, $\text{len}(\eta_\nu)$, can be significantly reduced; we refer to the corresponding models as ICTP_{sym}. Furthermore, the computational cost of the Cartesian product basis can be reduced by performing the calculations in the latent feature space. We use learnable weights $W_{kk'l_\xi}$ to reduce the number of feature channels for the product basis calculation and then increase it again for subsequent steps. For more details on the model architecture, such as the construction of updated many-body node embeddings, readout functions, and different options for the Cartesian product basis, see Appendix B.2.

Runtime considerations. When choosing an architecture to implement MLIPs, the runtime per force and energy evaluation is crucial. The asymptotic time complexity as a function of rank L is $\mathcal{O}(9^L L! / (2^{L/2} (L/2)!))$ for irreducible Cartesian tensors and $\mathcal{O}(L^6)$ for spherical ones; see Appendix B.3 for more details. Thus, spherical tensors are more computationally efficient for $L \rightarrow \infty$. However, state-of-the-art models and physical properties typically require $L \leq 4$ [33, 78], making sub-leading terms and implementation-dependent amplitudes crucial. Based on our analysis, for $L \leq 4$, we can expect models based on irreducible Cartesian tensors to be more computationally

Table 1: **Energy (E) and force (F) mean absolute errors (MAEs) for the rMD17 data set.** E- and F-MAE are provided in meV and meV/Å, respectively. Results are presented for models trained using $N_{\text{train}} = 950$ and $N_{\text{train}} = 50$ configurations randomly drawn from the data set. Further 50 configurations are used for early stopping. All values are obtained by averaging over five independent runs, with the standard deviation provided if available. Best performances, considering the standard deviation, are highlighted in bold.

		$N_{\text{train}} = 950$					$N_{\text{train}} = 50$		
		ICTP _{sym}	TensorNet [30]	MACE [33]	Allegro [34]	NequIP [25]	NequIP [25]	MACE [33]	ICTP _{sym}
Aspirin	E	2.27 ± 0.11	2.4	2.2	2.3	2.3	19.5	17.0	14.84 ± 0.98
	F	6.67 ± 0.19	8.9 ± 0.1	6.6	7.3	8.2	52.0	43.9	40.19 ± 0.95
Azobenzene	E	1.20 ± 0.01	0.7	1.2	1.2	0.7	6.0	5.4	5.47 ± 0.63
	F	2.92 ± 0.03	3.1	3.0	2.6	2.9	20.0	17.7	17.25 ± 0.53
Benzene	E	0.26 ± 0.00	0.02	0.4	0.3	0.04	0.6	0.7	0.38 ± 0.02
	F	0.34 ± 0.02	0.3	0.3	0.2	0.3	2.9	2.7	2.45 ± 0.13
Ethanol	E	0.43 ± 0.02	0.5	0.4	0.4	0.4	8.7	6.7	6.15 ± 0.26
	F	2.63 ± 0.10	3.5	2.1	2.1	2.8	40.2	32.6	29.53 ± 1.14
Malonaldehyde	E	0.82 ± 0.03	0.8	0.8	0.6	0.8	12.7	10.0	9.72 ± 0.42
	F	4.96 ± 0.21	5.4	4.1	3.6	5.1	52.5	43.3	42.88 ± 3.08
Naphthalene	E	0.56 ± 0.00	0.2	0.5	0.2	0.9	2.1	2.1	2.06 ± 0.10
	F	1.45 ± 0.05	1.6	1.6	0.9	1.3	10.0	9.2	9.43 ± 0.46
Paracetamol	E	1.44 ± 0.03	1.3	1.3	1.5	1.4	14.3	9.7	8.94 ± 0.66
	F	4.89 ± 0.11	5.9 ± 0.1	4.8	4.9	5.9	39.7	31.5	30.13 ± 1.51
Salicylic acid	E	0.97 ± 0.01	0.8	0.9	0.9	0.7	8.0	6.5	5.95 ± 0.43
	F	3.66 ± 0.06	4.6 ± 0.1	3.1	2.9	4.0	35.9	28.4	27.78 ± 1.93
Toluene	E	0.46 ± 0.00	0.3	0.5	0.4	0.3	3.3	3.1	2.45 ± 0.13
	F	1.61 ± 0.02	1.7	1.5	1.8	1.6	15.1	12.1	11.24 ± 0.55
Uracil	E	0.57 ± 0.01	0.4	0.5	0.6	0.4	7.3	4.4	4.66 ± 0.16
	F	2.64 ± 0.08	3.1	2.1	1.8	3.1	40.1	25.9	25.97 ± 0.78

and memory efficient than their spherical counterparts. Nonetheless, it is essential to consider the inference times for a fair comparison, which we provide in Section 5.

Equivariance of message-passing layers. We conclude this section by giving a theoretical result that ensures the equivariance of message-passing layers based on irreducible Cartesian tensors and their irreducible tensor products to actions of the orthogonal group. The proof is provided in Appendix C.

Proposition 4.1. *The message-passing layers based on irreducible Cartesian tensors and their irreducible tensor products are equivariant to actions of the orthogonal group.*

5 Experiments and results

This section presents the results for the three benchmark data sets: rMD17, 3BPA, and acetylacetone. We describe data sets and training details in Appendix D.1 and Appendix D.2, respectively.

Molecular dynamics trajectories. We assess the performance of ICTP models using the revised MD17 data set, which includes structures, total energies, and atomic forces for ten small organic molecules obtained from ab initio molecular dynamics simulations [47]. Table 1 shows that ICTP_{sym} achieves accuracy on par with state-of-the-art spherical and Cartesian models. Notably, several methods exhibit similar accuracy when trained with 950 configurations. However, the achieved accuracy is much lower than the desired accuracy of $43.37 \text{ meV} \approx 1 \text{ kcal/mol}$, making a model comparison less meaningful. Therefore, we also compare ICTP_{sym} with MACE and NequIP, trained using 50 configurations, making learning accurate MLIPs more challenging. From Table 1, we see that ICTP_{sym} outperforms MACE and NequIP for most molecules in this scenario.

Extrapolation to out-of-domain data. We further assess the performance of ICTP models using the 3BPA data set [48]. The training data set comprises 500 configurations, total energies, and atomic forces acquired from molecular dynamics at 300 K. The test data set is obtained from simulations at 300 K, 600 K, and 1200 K. We also test our models using energies and forces along dihedral rotations of the molecule. Table 2 shows that ICTP models trained using 450 configurations perform on par with state-of-the-art spherical models, similar to the results for rMD17. However, we were not able to reproduce the original results using the current MACE source code and the described training setup [33]. Therefore, for a fair comparison, we unified the training setup for ICTP and MACE (see

Table 2: **Energy (E) and force (F) root-mean-square errors (RMSEs) for the 3BPA data set.** E- and F-RMSE are provided in meV and meV/Å, respectively. Results are presented for models trained using 450 configurations randomly drawn from the training data set collected at 300 K, while the remaining 50 are used for early stopping. All values for ICTP models are obtained by averaging over five independent runs. For MACE and NequIP, the results are reported for three independent runs. The standard deviation is provided if it is available. Best performances, considering the standard deviation, are highlighted in bold. Inference time and memory consumption are measured for a batch size of 100. Inference time is reported per structure in ms, while memory consumption is provided for the entire batch in GB.

		ICTP _{full}	ICTP _{sym}	ICTP _{sym+lt}	MACE ^a	CACE [31]	MACE [33]	NequIP [34]
300 K	E	2.70 ± 0.22	2.70 ± 0.08	2.98 ± 0.34	2.81 ± 0.18	6.3	3.0 ± 0.2	3.28 ± 0.10
	F	9.45 ± 0.29	9.39 ± 0.31	9.57 ± 0.20	9.47 ± 0.42	21.4	8.8 ± 0.3	10.77 ± 0.19
600 K	E	10.74 ± 0.31	10.38 ± 0.80	10.29 ± 0.90	11.11 ± 1.41	18.0	9.7 ± 0.5	11.16 ± 0.14
	F	22.99 ± 0.64	22.87 ± 0.91	23.03 ± 0.76	23.27 ± 1.45	45.2	21.8 ± 0.6	26.37 ± 0.09
1200 K	E	29.80 ± 0.92	30.84 ± 1.87	31.32 ± 1.80	31.15 ± 1.58	58.0	29.8 ± 1.0	38.52 ± 1.63
	F	62.82 ± 1.23	64.54 ± 3.88	65.36 ± 3.47	65.22 ± 3.52	113.8	62.0 ± 0.7	76.18 ± 1.11
Dihedral slices	E	9.82 ± 0.79	10.64 ± 1.07	13.03 ± 3.44	8.56 ± 1.53	–	7.8 ± 0.6	23.2 [33]
	F	17.52 ± 0.54	17.18 ± 0.81	19.31 ± 0.83	17.69 ± 1.29	–	16.5 ± 1.7	23.1 [33]
Inference time		6.45 ± 0.50	5.31 ± 0.02	3.51 ± 0.22	4.66 ± 0.05	–	24.3^b	103.5 ^b [33]
Memory consumption		49.66 ± 0.00	42.01 ± 0.11	39.08 ± 0.00	36.26 ± 0.00	–	–	–

^a During inference time measurements with the MACE source code, we were not able to reproduce the original results [33]. Thus, we re-run MACE experiments using the same training setup as for ICTP; see Appendix D.2.

^b The original publication did not report the batch size used to measure inference time [33]. Therefore, the values provided are used solely to demonstrate the relative computational cost of MACE and NequIP.

Appendix D.2) and Table 2 reports the corresponding results for 450 training configurations. In Table A1, we present the results obtained for ICTP and MACE trained using 50 configurations.

From Table 2, we observe that ICTP_{full} slightly outperforms MACE in total energy and atomic force RMSEs but is ~ 1.4 times less computationally efficient. This difference arises from MACE using the generalized Clebsch–Gordan coefficients and pre-computing their product with the weights in the linear expansion (i.e., weights of Eq. (A1)) [33], which reduces the effective number of evaluated tensor products. For example, MACE computes six tensor products for constructing the product basis in the first message-passing layer, whereas ICTP_{full} computes 124. Thus, ICTP_{full}’s lower computational efficiency can be explained by the use of the MACE architecture, which has been chosen to provide a fair comparison between irreducible Cartesian and spherical tensors. Using the symmetric Cartesian product basis and that in the latent space, we further improve the runtime of our models while maintaining accuracy on par with MACE. Regarding memory consumption, MACE and ICTP perform similarly despite the larger number of tensor products required for computing the Cartesian product basis in Eq. (6). This observation can be attributed to the Clebsch–Gordan tensor product requiring the computation of intermediate tensors $\mathbf{Y}^L \otimes \mathbf{Y}^L \in \mathbb{R}^{(2L+1) \times (2L+1)}$ with $(2L+1)^2$ elements, while irreducible Cartesian tensors use $\mathbf{T}_L \in (\mathbb{R}^3)^{\otimes L}$ with 3^L elements.

Figure 2 compares potential energy profiles obtained with ICTP and MACE trained using 50 configurations. For the potential energy cut at $\beta = 180^\circ$ (left panel), ICTP and MACE perform similarly, except for the energy barrier at $\gamma \approx 143^\circ$, which ICTP tends to underestimate stronger than MACE. For $\beta = 150^\circ$ (middle panel), however, ICTP_{full} and ICTP_{sym} outperform MACE across nearly the entire range of the dihedral angle γ . For $\beta = 180^\circ$ (right panel), all models perform similarly. Figure A1 shows the corresponding potential energy profiles for models trained with 450 configurations. All models perform similarly in this scenario, with energy profiles close to the reference (DFT).

Flexibility and reactivity. We further use the acetylacetone data set to assess the ICTP models’ extrapolation capabilities to higher temperatures (similar to 3BPA), bond breaking, and bond torsions [32]. Table 3 shows that ICTP models achieve state-of-the-art results while employing fewer parameters than spherical counterparts. Appendix D.3 includes additional results for the acetylacetone data set, such as total energy and atomic force RMSEs for models trained with 50 configurations and details on the potential energy profiles for hydrogen transfer and C-C bond rotation. Overall, ICTP and MACE perform similarly, demonstrating excellent generalization capability. However, when

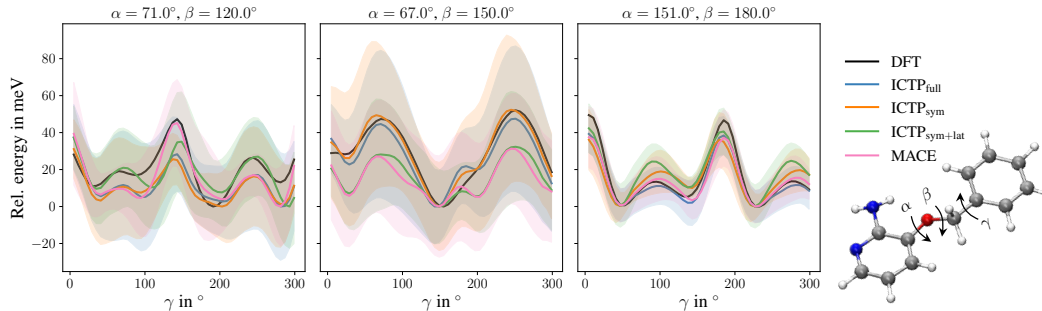


Figure 2: **Potential energy profiles for three cuts through the 3BPA molecule’s potential energy surface.** All models are trained using 50 configurations, and additional 50 are used for early stopping. The 3BPA molecule, including the three dihedral angles (α , β , and γ), provided in degrees $^\circ$, is shown as an inset. The color code of the inset molecule is C grey, O red, N blue, and H white. The reference potential energy profile (DFT) is shown in black. Each profile is shifted such that each model’s lowest energy is zero. Shaded areas denote standard deviations across five independent runs.

Table 3: **Energy (E) and force (F) root-mean-square errors (RMSEs) for the acetylacetone data set.** E- and F-RMSE are provided in meV and meV/Å, respectively. Results are presented for models trained using 450 configurations randomly drawn from the training data set collected at 300 K, while the remaining 50 are used for early stopping. All values for ICTP models are obtained by averaging over five independent runs. For MACE and NequIP, the results are reported for three independent runs. The standard deviation is provided if it is available. Best performances, considering the standard deviation, are highlighted in bold.

		ICTP _{full}	ICTP _{sym}	ICTP _{sym+lt}	MACE ^a	MACE [33]	NequIP [32]
300 K	E	0.75 ± 0.04	0.76 ± 0.03	0.77 ± 0.04	0.75 ± 0.05	0.9 ± 0.03	0.81 ± 0.05
	F	5.08 ± 0.11	5.17 ± 0.10	5.18 ± 0.16	5.00 ± 0.17	5.1 ± 0.10	5.90 ± 0.46
600 K	E	5.39 ± 1.22	4.43 ± 0.34	5.12 ± 0.29	4.96 ± 0.64	4.6 ± 0.3	6.04 ± 1.54
	F	23.21 ± 1.96	22.90 ± 1.62	24.05 ± 1.71	23.25 ± 1.82	22.4 ± 0.9	27.8 ± 4.03
Number of parameters		2,774,800	2,736,400	2,648,080	2,803,984	2,803,984	3,190,488

^a Similar to Table 2, we re-run MACE experiments using the same training setup as for ICTP; see Appendix D.2.

trained using 50 configurations, ICTP_{full} is the only MLIP consistently producing the potential energy profile for hydrogen transfer close to the reference (DFT).

6 Conclusions and limitations

This work introduces many-body equivariant MPNNs based on higher-rank irreducible Cartesian tensors, offering an alternative to spherical models. We assess the performance of resulting MPNNs using molecular benchmark data sets, such as rMD17, 3BPA, and acetylacetone. In these experiments, MPNNs based on irreducible Cartesian tensors show a lower computational cost of individual operations compared to spherical counterparts. Furthermore, we demonstrate that these Cartesian models achieve accuracy and generalization capability on par with or better than state-of-the-art spherical models while memory consumption is comparable. Our results hold across the typical range of tensor ranks used in modeling many-body interactions and relevant physical properties, i.e., $L \leq 4$.

Limitations. We emphasize our focus on introducing MPNNs based on irreducible Cartesian tensors and prove their equivariance. We adapted the MACE architecture, which uses only tensors of even parity, to enable a fair comparison with spherical models. Further modifications to the architecture are possible, which we expect to exploit the full potential of irreducible Cartesian tensors. Future work should also extend the assessment of MPNNs based on irreducible Cartesian tensors using larger and more diverse atomic systems.

Code availability

The source code will be made publicly available upon publication.

Acknowledgements

MN acknowledges support from the Deutsche Forschungsgemeinschaft (DFG, German Research Foundation) under Germany’s Excellence Strategy - EXC 2075 – 390740016 and the Stuttgart Center for Simulation Science (SimTech).

References

- [1] K. T. Butler, D. W. Davies, H. Cartwright, O. Isayev, and A. Walsh: *Machine learning for molecular and materials science*. Nature **559**, 547–555 (2018)
- [2] J. Vamathevan, D. Clark, P. Czodrowski, I. Dunham, E. Ferran et al.: *Applications of machine learning in drug discovery and development*. Nat. Rev. Drug Discov. **18**, 463–477 (2019)
- [3] J. A. Keith, V. Vassilev-Galindo, B. Cheng, S. Chmiela, M. Gastegger et al.: *Combining Machine Learning and Computational Chemistry for Predictive Insights Into Chemical Systems*. Chem. Rev. **121**, 9816–9872 (2021)
- [4] O. T. Unke, S. Chmiela, H. E. Sauceda, M. Gastegger, I. Poltavsky et al.: *Machine Learning Force Fields*. Chem. Rev. **121**, 10142–10186 (2021)
- [5] N. Fedik, R. Zubatyuk, M. Kulichenko, N. Lubbers, J. S. Smith et al.: *Extending machine learning beyond interatomic potentials for predicting molecular properties*. Nat. Rev. Chem. **6**, 653–672 (2022)
- [6] A. Merchant, S. Batzner, S. S. Schoenholz, M. Aykol, G. Cheon et al.: *Scaling deep learning for materials discovery*. Nature **624**, 80–85 (2023)
- [7] D. P. Kovács, J. H. Moore, N. J. Browning, I. Batatia, J. T. Horton et al.: *MACE-OFF23: Transferable Machine Learning Force Fields for Organic Molecules*. <https://arxiv.org/abs/2312.15211> (2023)
- [8] I. Batatia, P. Benner, Y. Chiang, A. M. Elena, D. P. Kovács et al.: *A foundation model for atomistic materials chemistry*. <https://arxiv.org/abs/2401.00096> (2023)
- [9] G. D. Purvis and R. J. Bartlett: *A full coupled-cluster singles and doubles model: The inclusion of disconnected triples*. J. Chem. Phys. **76**, 1910–1918 (1982)
- [10] T. D. Crawford and H. F. Schaefer III: *An Introduction to Coupled Cluster Theory for Computational Chemists*, pp. 33–136. John Wiley & Sons, Ltd (2000)
- [11] R. J. Bartlett and M. Musiał: *Coupled-cluster theory in quantum chemistry*. Rev. Mod. Phys. **79**, 291–352 (2007)
- [12] P. Hohenberg and W. Kohn: *Inhomogeneous Electron Gas*. Phys. Rev. **136**, B864–B871 (1964)
- [13] W. Kohn and L. J. Sham: *Self-Consistent Equations Including Exchange and Correlation Effects*. Phys. Rev. **140**, A1133–A1138 (1965)
- [14] A. Micheli: *Neural network for graphs: A contextual constructive approach*. IEEE Trans. Neural Netw. **20**, 498–511 (2009)
- [15] F. Scarselli, M. Gori, A. C. Tsoi, M. Hagenbuchner, and G. Monfardini: *The graph neural network model*. IEEE Trans. Neural Netw. **20**, 61–80 (2009)
- [16] J. Gilmer, S. S. Schoenholz, P. F. Riley, O. Vinyals, and G. E. Dahl: *Neural Message Passing for Quantum Chemistry*. Int. Conf. Mach. Learn. **70**, 1263–1272 (2017)

- [17] W. L. Hamilton, R. Ying, and J. Leskovec: *Representation learning on graphs: Methods and applications*. IEEE Data Eng. Bull. **40**, 52–74 (2017)
- [18] M. M. Bronstein, J. Bruna, Y. LeCun, A. Szlam, and P. Vandergheynst: *Geometric deep learning: going beyond Euclidean data*. IEEE Signal Process. Mag. **34**, 18–42 (2017)
- [19] Z. Zhang, P. Cui, and W. Zhu: *Deep Learning on Graphs: A Survey*. IEEE Trans. Knowl. Data Eng. **34**, 249–270 (2022)
- [20] S. Zhang, H. Tong, J. Xu, and R. Maciejewski: *Graph convolutional networks: a comprehensive review*. Comput. Soc. Netw. **6**, 11 (2019)
- [21] D. Bacciu, F. Errica, A. Micheli, and M. Podda: *A Gentle Introduction to Deep Learning for Graphs*. Neural Netw. **129**, 203–221 (2020)
- [22] C. L. Zitnick, L. Chanussot, A. Das, S. Goyal, J. Heras-Domingo et al.: *An Introduction to Electrocatalyst Design using Machine Learning for Renewable Energy Storage*. <https://arxiv.org/abs/2010.09435> (2020)
- [23] J. Jumper, R. Evans, A. Pritzel, T. Green, M. Figurnov et al.: *Highly accurate protein structure prediction with AlphaFold*. Nature **596**, 583–589 (2021)
- [24] J. Dauparas, I. Anishchenko, N. Bennett, H. Bai, R. J. Ragotte et al.: *Robust deep learning-based protein sequence design using ProteinMPNN*. Science **378**, 49–56 (2022)
- [25] S. Batzner, A. Musaelian, L. Sun, M. Geiger, J. P. Mailoa et al.: *$E(3)$ -equivariant graph neural networks for data-efficient and accurate interatomic potentials*. Nat. Commun. **13**, 2453 (2022)
- [26] A. Duval, S. V. Mathis, C. K. Joshi, V. Schmidt, S. Miret et al.: *A Hitchhiker’s Guide to Geometric GNNs for 3D Atomic Systems*. <https://arxiv.org/abs/2312.07511> (2024)
- [27] M. F. Langer, A. Goeßmann, and M. Rupp: *Representations of molecules and materials for interpolation of quantum-mechanical simulations via machine learning*. npj Comput. Mater. **8**, 41 (2022)
- [28] K. T. Schütt, O. T. Unke, and M. Gastegger: *Equivariant message passing for the prediction of tensorial properties and molecular spectra*. Int. Conf. Mach. Learn. **139**, 9377–9388 (2021)
- [29] M. Haghighatlari, J. Li, X. Guan, O. Zhang, A. Das et al.: *NewtonNet: a Newtonian message passing network for deep learning of interatomic potentials and forces*. Digital Discovery **1**, 333–343 (2022)
- [30] G. Simeon and G. D. Fabritiis: *TensorNet: Cartesian Tensor Representations for Efficient Learning of Molecular Potentials*. Adv. Neural Inf. Process. Syst. **36**, 37334–37353 (2023)
- [31] B. Cheng: *Cartesian atomic cluster expansion for machine learning interatomic potentials*. <https://arxiv.org/abs/2402.07472> (2024)
- [32] I. Batatia, S. Batzner, D. P. Kovács, A. Musaelian, G. N. C. Simm et al.: *The Design Space of $E(3)$ -Equivariant Atom-Centered Interatomic Potentials*. <https://arxiv.org/abs/2205.06643> (2022)
- [33] I. Batatia, D. P. Kovacs, G. N. C. Simm, C. Ortner, and G. Csanyi: *MACE: Higher Order Equivariant Message Passing Neural Networks for Fast and Accurate Force Fields*. Adv. Neural Inf. Process. Syst. **35**, 11423–11436 (2022)
- [34] A. Musaelian, S. Batzner, A. Johansson, L. Sun, C. J. Owen et al.: *Learning local equivariant representations for large-scale atomistic dynamics*. Nat. Commun. **14**, 579 (2023)
- [35] S. Passaro and C. L. Zitnick: *Reducing $SO(3)$ Convolutions to $SO(2)$ for Efficient Equivariant GNNs*. Int. Conf. Mach. Learn. **202**, 27420–27438 (2023)
- [36] S. Luo, T. Chen, and A. S. Krishnapriyan: *Enabling Efficient Equivariant Operations in the Fourier Basis via Gaunt Tensor Products*. Int. Conf. Learn. Represent. <https://arxiv.org/abs/2401.10216> (2024)

- [37] P. Thölke and G. D. Fabritiis: *Equivariant Transformers for Neural Network based Molecular Potentials*. Int. Conf. Learn. Represent. <https://arxiv.org/abs/2202.02541> (2022)
- [38] R. F. Snider: *Irreducible Cartesian Tensors*. De Gruyter, Berlin, Boston (2018)
- [39] N. Thomas, T. Smidt, S. Kearnes, L. Yang, L. Li et al.: *Tensor field networks: Rotation- and translation-equivariant neural networks for 3D point clouds*. <https://arxiv.org/abs/1802.08219> (2018)
- [40] R. Drautz: *Atomic cluster expansion for accurate and transferable interatomic potentials*. Phys. Rev. B **99**, 014104 (2019)
- [41] E. Wigner: *Group Theory and its Application to the Quantum Mechanics of Atomic Spectra*, volume 5. Elsevier (2012)
- [42] J. A. R. Coope, R. F. Snider, and F. R. McCourt: *Irreducible Cartesian Tensors*. J. Chem. Phys. **43**, 2269–2275 (1965)
- [43] J. A. R. Coope and R. F. Snider: *Irreducible Cartesian Tensors. II. General Formulation*. J. Math. Phys. **11**, 1003–1017 (1970)
- [44] J. A. R. Coope: *Irreducible Cartesian Tensors. III. Clebsch-Gordan Reduction*. J. Math. Phys. **11**, 1591–1612 (1970)
- [45] D. R. Lehman and W. C. Parke: *Angular reduction in multiparticle matrix elements*. J. Math. Phys. **30**, 2797–2806 (1989)
- [46] M. Weiler, M. Geiger, M. Welling, W. Boomsma, and T. S. Cohen: *3D Steerable CNNs: Learning Rotationally Equivariant Features in Volumetric Data*. Adv. Neural Inf. Process. Syst. **31** (2018)
- [47] A. S. Christensen and O. A. von Lilienfeld: *On the role of gradients for machine learning of molecular energies and forces*. Mach. Learn.: Sci. Technol. **1**, 045018 (2020)
- [48] D. P. Kovács, C. v. d. Oord, J. Kucera, A. E. A. Allen, D. J. Cole et al.: *Linear Atomic Cluster Expansion Force Fields for Organic Molecules: Beyond RMSE*. J. Chem. Theory Comput. **17**, 7696–7711 (2021)
- [49] R. Drautz: *Atomic cluster expansion of scalar, vectorial, and tensorial properties including magnetism and charge transfer*. Phys. Rev. B **102**, 024104 (2020)
- [50] A. V. Shapeev: *Moment Tensor Potentials: A Class of Systematically Improvable Interatomic Potentials*. Multiscale Model. Simul. **14**, 1153–1173 (2016)
- [51] J. Behler and M. Parrinello: *Generalized Neural-Network Representation of High-Dimensional Potential-Energy Surfaces*. Phys. Rev. Lett. **98**, 146401 (2007)
- [52] J. Behler: *Atom-centered symmetry functions for constructing high-dimensional neural network potentials*. J. Chem. Phys. **134**, 074106 (2011)
- [53] A. P. Bartók, M. C. Payne, R. Kondor, and G. Csányi: *Gaussian Approximation Potentials: The Accuracy of Quantum Mechanics, without the Electrons*. Phys. Rev. Lett. **104**, 136403 (2010)
- [54] A. P. Bartók, R. Kondor, and G. Csányi: *On representing chemical environments*. Phys. Rev. B **87**, 184115 (2013)
- [55] V. Zaverkin and J. Kästner: *Gaussian Moments as Physically Inspired Molecular Descriptors for Accurate and Scalable Machine Learning Potentials*. J. Chem. Theory Comput. **16**, 5410–5421 (2020)
- [56] V. Zaverkin, D. Holzmüller, I. Steinwart, and J. Kästner: *Fast and Sample-Efficient Interatomic Neural Network Potentials for Molecules and Materials Based on Gaussian Moments*. J. Chem. Theory Comput. **17**, 6658–6670 (2021)

- [57] M. S. Daw and M. I. Baskes: *Embedded-atom method: Derivation and application to impurities, surfaces, and other defects in metals*. Phys. Rev. B **29**, 6443–6453 (1984)
- [58] Y.-M. Kim, B.-J. Lee, and M. I. Baskes: *Modified embedded-atom method interatomic potentials for Ti and Zr*. Phys. Rev. B **74**, 014101–014112 (2006)
- [59] A. Stone: *Transformation between cartesian and spherical tensors*. Mol. Phys. **29**, 1461–1471 (1975)
- [60] A. J. Stone: *Properties of Cartesian-spherical transformation coefficients*. J. Phys. A **9**, 485 (1976)
- [61] J. M. Normand and J. Raynal: *Relations between Cartesian and spherical components of irreducible Cartesian tensors*. J. Phys. A **15**, 1437 (1982)
- [62] B. Anderson, T. S. Hy, and R. Kondor: *Cormorant: Covariant Molecular Neural Networks*. Adv. Neural Inf. Process. Syst. **32**, 14537–14546 (2019)
- [63] V. G. Satorras, E. Hoogeboom, and M. Welling: *E(n) Equivariant Graph Neural Networks*. Int. Conf. Mach. Learn. **139**, 9323–9332 (2021)
- [64] J. Brandstetter, R. Hesselink, E. van der Pol, E. J. Bekkers, and M. Welling: *Geometric and Physical Quantities improve E(3) Equivariant Message Passing*. Int. Conf. Learn. Represent. <https://arxiv.org/abs/2110.02905> (2022)
- [65] K. Schütt, P.-J. Kindermans, H. E. Sauceda Felix, S. Chmiela, A. Tkatchenko et al.: *SchNet: A continuous-filter convolutional neural network for modeling quantum interactions*. Adv. Neural Inf. Process. Syst. **30**, 991–1001 (2017)
- [66] O. T. Unke and M. Meuwly: *PhysNet: A Neural Network for Predicting Energies, Forces, Dipole Moments, and Partial Charges*. J. Chem. Theory Comput. **15** (6), 3678–3693 (2019)
- [67] Y. Liu, L. Wang, M. Liu, Y. Lin, X. Zhang et al.: *Spherical Message Passing for 3D Molecular Graphs*. Int. Conf. Learn. Represent. <https://arxiv.org/abs/2102.05013> (2022)
- [68] J. Gasteiger, S. Giri, J. T. Margraf, and S. Günnemann: *Fast and Uncertainty-Aware Directional Message Passing for Non-Equilibrium Molecules*. Machine Learning for Molecules Workshop, Adv. Neural Inf. Process. Syst. <https://arxiv.org/abs/2011.14115> (2020)
- [69] J. Gasteiger, F. Becker, and S. Günnemann: *GemNet: Universal Directional Graph Neural Networks for Molecules*. Adv. Neural Inf. Process. Syst. **34**, 6790–6802 (2021)
- [70] J. Gasteiger, J. Groß, and S. Günnemann: *Directional Message Passing for Molecular Graphs*. Int. Conf. Learn. Represent. <https://arxiv.org/abs/2003.03123> (2020)
- [71] D. P. Kovács, I. Batatia, E. S. Arany, and G. Csányi: *Evaluation of the MACE force field architecture: From medicinal chemistry to materials science*. J. Chem. Phys. **159**, 044118 (2023)
- [72] F. Fuchs, D. Worrall, V. Fischer, and M. Welling: *SE(3)-Transformers: 3D Roto-Translation Equivariant Attention Networks*. Adv. Neural Inf. Process. Syst. **33**, 1970–1981 (2020)
- [73] T. Frank, O. Unke, and K.-R. Müller: *So3krates: Equivariant attention for interactions on arbitrary length-scales in molecular systems*. Adv. Neural Inf. Process. Syst. **35**, 29400–29413 (2022)
- [74] Y.-L. Liao, B. Wood, A. Das, and T. Smidt: *EquiformerV2: Improved Equivariant Transformer for Scaling to Higher-Degree Representations*. Int. Conf. Learn. Represent. <https://arxiv.org/abs/2306.12059> (2023)
- [75] U. Fano and G. Racah: *Irreducible Tensorial Sets*. Academic Press Inc., New York (1959)
- [76] I. M. Gel’fand, R. A. Minlos, and Z. Y. Shapiro: *Representations of the Rotation and Lorentz Groups and Their Applications*. Pergamon Press, Inc. (1963)

- [77] S. V. S. Martin H. Müser and L. Pastewka: *Interatomic potentials: achievements and challenges*. Adv. Phys. X **8**, 2093129 (2023)
- [78] I. Grega, I. Batatia, G. Csanyi, S. Karlapati, and V. Deshpande: *Energy-conserving equivariant GNN for elasticity of lattice architected metamaterials*. Int. Conf. Learn. Represent. <https://arxiv.org/abs/2401.16914> (2024)
- [79] K. He, X. Zhang, S. Ren, and J. Sun: *Deep Residual Learning for Image Recognition*. IEEE Conf. Comput. Vis. Pattern Recognit. <https://doi.org/10.1109/CVPR.2016.90> (2016)
- [80] S. Chmiela, A. Tkatchenko, H. E. Sauceda, I. Poltavsky, K. T. Schütt et al.: *Machine learning of accurate energy-conserving molecular force fields*. Sci. Adv. **3**, e1603015 (2017)
- [81] K. T. Schütt, F. Arbabzadah, S. Chmiela, K. R. Müller, and A. Tkatchenko: *Quantum-chemical insights from deep tensor neural networks*. Nat. Commun. **8**, 13890 (2017)
- [82] S. Chmiela, H. E. Sauceda, K.-R. Müller, and A. Tkatchenko: *Towards exact molecular dynamics simulations with machine-learned force fields*. Nat. Commun. **9**, 3887 (2018)
- [83] S. Elfving, E. Uchibe, and K. Doya: *Sigmoid-Weighted Linear Units for Neural Network Function Approximation in Reinforcement Learning*. Neural Netw. **107**, 3–11 (2018)
- [84] P. Ramachandran, B. Zoph, and Q. V. Le: *Searching for activation functions*. Int. Conf. Learn. Represent. <https://arxiv.org/abs/1710.05941> (2018)
- [85] S. J. Reddi, S. Kale, and S. Kumar: *On the Convergence of Adam and Beyond*. Int. Conf. Learn. Represent. <https://arxiv.org/abs/1904.09237> (2018)

A Background

Message-passing neural networks. Message-passing neural networks (MPNNs) learn node representations in a graph by iteratively processing local information sent by the nodes' neighbors. The initial features of node u are represented as the vector \mathbf{x}_u , and undirected edges $\{u, v\}$ connect pairs of nodes u, v . A node v belongs to the neighborhood of node u , denoted as $\mathcal{N}(u)$, if there exists an edge $\{u, v\}$ in the graph. Typically, the $(t + 1)$ -th message-passing layer computes a new node u 's representation $\mathbf{h}_u^{(t+1)}$ by applying a permutation invariant aggregation function over the neighbors [16, 21]

$$\mathbf{h}_u^{(t+1)} = \phi^{(t)}\left(\mathbf{h}_u^{(t)}, \sum_{v \in \mathcal{N}(u)} \psi^{(t)}(\mathbf{h}_u^{(t)}, \mathbf{h}_v^{(t)})\right),$$

where $\phi^{(t)}, \psi^{(t)}$ are often implemented as learnable fully-connected neural networks (NNs), and $\mathbf{h}_u^{(0)} = \mathbf{x}_u$. To learn a mapping from a learned representation $\mathbf{h}_u^{(t)}$ to the atoms' energies, we can couple T message-passing layers with corresponding readout functions \mathcal{R}_t , $t \in \{1, \dots, T\}$ such that $E_u = \sum_{t=1}^T \mathcal{R}_t(\mathbf{h}_u^{(t)})$.

Many-body interatomic potentials. Interatomic potentials approximate the potential energy of atoms—the electronic ground state energy—as a function of their coordinates [77]. Many-body potentials naturally arise because the interaction between two atoms is influenced by the presence of additional atoms, changing their electronic structure. This concept is formalized by expanding the atomic energy E_u of a many-atom system into a series of two-body, three-body, and higher-body-order contributions

$$E_u = E^{(1)}(\mathbf{r}_u) + \sum_{v_1} E^{(2)}(\mathbf{r}_u, \mathbf{r}_{v_1}) + \sum_{v_1 < v_2} E^{(3)}(\mathbf{r}_u, \mathbf{r}_{v_1}, \mathbf{r}_{v_2}) + \dots,$$

where \mathbf{r}_u represents the position of atom u and the superscript ν in $E^{(\nu)}$ indicates the order of the many-body interaction. In the absence of external fields, $E^{(\nu)}$ contributions to the atomic energy are invariant to rotations, and the two-body potential depends only on distances $r_{uv} = \|\mathbf{r}_u - \mathbf{r}_v\|_2$

$$E_u = \sum_{v_1} E^{(2)}(r_{uv_1}) + \sum_{v_1 < v_2} E^{(3)}(r_{uv_1}, r_{uv_2}, r_{v_1 v_2}) + \dots$$

Expansions of this form have found a broad application in constructing machine-learned interatomic potentials (MLIPs), significantly advancing the field [40, 50].

Many-body message passing. Designing accurate and computationally efficient interatomic potential models for interacting many-body systems requires including higher-body-order energy contributions and, thus, higher-body-order learnable features. Recently, a new message construction mechanism has been proposed by expanding the messages $\mathbf{m}_u^{(t)}$ to include many-body contributions [33]

$$\mathbf{m}_u^{(t)} = \sum_{v_1} \psi_2^{(t)}(\mathbf{h}_u^{(t)}, \mathbf{h}_{v_1}^{(t)}) + \sum_{v_1, v_2} \psi_3^{(t)}(\mathbf{h}_u^{(t)}, \mathbf{h}_{v_1}^{(t)}, \mathbf{h}_{v_2}^{(t)}) + \dots + \sum_{v_1, \dots, v_\nu} \psi_{\nu+1}^{(t)}(\mathbf{h}_u^{(t)}, \mathbf{h}_{v_1}^{(t)}, \dots, \mathbf{h}_{v_\nu}^{(t)}),$$

where $(\nu + 1)$ denotes the order of many-body interactions, defining the number of contracted tensors. Using \sum_{v_1, \dots, v_ν} instead of $\sum_{v_1 < \dots < v_\nu}$ circumvents the exponential increase in computational cost with ν . It allows exploiting the product structure of many-body features, which differs from other approaches [68–70].

B Methods

B.1 Normalization constants

The following provides the normalization constants $C_{l_1 l_2 l_3}$ and $D_{l_1 l_2 l_3}$ for even and odd irreducible Cartesian tensor products in Eqs. (2) and (3), respectively. The respective normalization constants read [45]

$$C_{l_1 l_2 l_3} = \frac{l_1! l_2! (2l_3 - 1)!! ((L_1 + 1)/2)! ((L_2 + 1)/2)!}{l_3! L_1! L_2! L_3! (L/2)!},$$

$$D_{l_1 l_2 l_3} = \frac{2l_1! l_2! (2l_3 - 1)!! (L_1/2)! (L_2/2)!}{(l_3 - 1)! (L_1 + 1)! (L_2 + 1)! (L_3 + 1)! ((L + 1)/2)!},$$

with $L = l_1 + l_2 + l_3$ and $L_i = L - 2l_i - 1$. Here, $C_{l_1 l_2 l_3}$ is defined such that an l_3 -fold contraction of the tensor \mathbf{z}_{l_3} , obtained through the irreducible Cartesian tensor product between \mathbf{x}_{l_1} and \mathbf{y}_{l_2} (\mathbf{x}_{l_1} and \mathbf{y}_{l_2} are obtained using Eq. (1)), with the unit vector $\hat{\mathbf{r}}$ yields unity. Please refer to the original publication for the motivation behind $D_{l_1 l_2 l_3}$ [45].

B.2 Further details on the equivariant message passing

The following provides additional details on the employed equivariant message-passing architecture. Learnable weights employed in Eqs. (4), (5), and (6) (i.e., $W_{kk'l_2}^{(t)}$, $W_{kZ_v}^{(t)}$, and $W_{kk'l_\xi}^{(t)}$ with k, k' running over feature channels) are initialized by picking the respective entries from a normal distribution with zero mean and unit variance.

Many-body message-passing. The many-body equivariant features, represented by an irreducible Cartesian tensor of rank L and obtained through the ν -fold tensor product in Eq. (6), are combined using the linear expansion

$$(\mathbf{m}_{ukL}^{(t)})_{i_1 i_2 \dots i_L} = \left(\sum_{\nu} \sum_{\eta_{\nu}} W_{Z_u \eta_{\nu} k L}^{(t)} \mathbf{B}_{u \eta_{\nu} k L}^{(t)} \right)_{i_1 i_2 \dots i_L}, \quad (\text{A1})$$

where $W_{Z_u k L \eta_{\nu}}^{(t)}$ denotes a learnable weight matrix which depends on the chemical element Z_u and rank L and which elements are initialized by picking the respective entries from a normal distribution with zero mean and variance of $1/\text{len}(\eta_{\nu})$. The updated node embeddings are further obtained as a linear function of $(\mathbf{m}_{ukL}^{(t)})_{i_1 i_2 \dots i_L}$ and the residual connection [33, 79]

$$(\mathbf{h}_{ukL}^{(t+1)})_{i_1 i_2 \dots i_L} = \frac{1}{\sqrt{d_t}} \sum_{k'} W_{kk'L}^{(t)} (\mathbf{m}_{ukL}^{(t)})_{i_1 i_2 \dots i_L} + \frac{1}{\sqrt{d_t N_Z}} \sum_{k'} W_{Z_u k k' L}^{(t)} (\mathbf{h}_{uk'L}^{(t)})_{i_1 i_2 \dots i_L}, \quad (\text{A2})$$

where N_Z denotes the number of atom types and learnable weights $W_{kk'L}^{(t)}$ and $W_{Z_u k k' L}^{(t)}$ are initialized by picking the respective entries from a normal distribution with zero mean and unit variance.

Full and symmetric product basis. In the MACE architecture, the authors pre-compute products between the generalized Clebsch–Gordan coefficients, which define the interaction between l_1 - and l_2 -rank spherical tensors, and the learnable weight $W_{Z_u \eta_{\nu} k L}^{(t)}$ of the linear expansion in Eq. (A1) [33]. This approach reduces the computational cost of constructing the product basis with spherical tensors as the effective number of evaluated tensor products is smaller. For irreducible Cartesian tensors, operations like matrix-vector and matrix-matrix products define the interaction between l_1 - and l_2 -rank tensors. Thus, an equivalent operation to those proposed for spherical tensors is generally impossible or would lead to an architecture different from MACE.

Note that one of our main goals is to demonstrate that a many-body equivariant message-passing architecture defined using higher-rank irreducible Cartesian tensors can be as expressive as the one using spherical tensors. Therefore, we compute $\mathbf{m}_{ukL}^{(t)}$ by directly evaluating the ν -fold tensor product, which effectively leads to a larger number of operations than for MACE. We refer to the models based on this architecture as irreducible Cartesian tensor potentials (ICTPs) with the full product basis, or $\text{ICTP}_{\text{full}}$. We also noticed that the number of tensor products, $\text{len}(\eta_{\nu})$, leading to the tensor of rank L , can be reduced by the symmetry of the two-fold tensor products, i.e., $\mathbf{A}_{l_1} \otimes \mathbf{A}_{l_2} = \mathbf{A}_{l_2} \otimes \mathbf{A}_{l_1}$ if \mathbf{A}_{l_1} and \mathbf{A}_{l_2} are symmetric. We refer to this design choice as ICTPs with the symmetric product basis or ICTP_{sym} .

Coupled and uncoupled feature channels. Using coupled feature channels instead of uncoupled ones in Eq. (A1) can improve the performance of the final model. Additionally, the number of feature channels and, thus, the overall computational cost can be reduced when constructing the product basis. However, the number of parameters and, thus, the expressiveness of the model can be preserved. Specifically, we can define a linear expansion for combining many-body equivariant features as

$$(\mathbf{m}_{ukL}^{(t)})_{i_1 i_2 \dots i_L} = \left(\sum_{\nu} \sum_{\eta_{\nu}} \sum_{k'} W_{Z_u \eta_{\nu} k k' L}^{(t)} \mathbf{B}_{u \eta_{\nu} k' L}^{(t)} \right)_{i_1 i_2 \dots i_L}, \quad (\text{A3})$$

where $W_{Z_u k k' L \eta_{\nu}}^{(t)}$ denotes a learnable weight matrix which depends on the chemical element Z_u and rank L and which elements are initialized by picking the respective entries from a normal distribution

with zero mean and variance of $1/(\sqrt{d_t} \times \text{len}(\eta_\nu))$. The construction of the product basis in the latent feature space requires encoding the two-body features $\mathbf{A}_{ukl\xi}^{(t)}$ using the learnable weight matrices in Eq. (6). The linear expansion is then constructed in the latent feature space and decoded using the learnable weight matrices of the linear function in Eq. (A2). We refer to this design choice as ICTPs with the product basis constructed in the latent feature space or ICTP_{lt}. Combining it with the symmetric product basis, we obtain ICTP_{sym+lt}.

Readout. Atomic energies expanded into a series of many-body contributions, $E_u = E_u^{(0)} + E_u^{(1)} + \dots + E_u^{(T)}$, are obtained by applying readout functions \mathcal{R}_t to node features with $L = 0$, which are invariant to rotations

$$E_u^{(t)} = \mathcal{R}_t\left(\{\mathbf{h}_{uk(L=0)}^{(t)}\}_k\right) = \begin{cases} \frac{1}{\sqrt{d_t}} \sum_{k'} W_{k'}^{(t)} h_{uk'(L=0)}^{(t)} & \text{if } t < T, \\ \text{NN}^{(t)}\left(\{\mathbf{h}_{uk(L=0)}^{(t)}\}_k\right) & \text{if } t = T, \end{cases} \quad (\text{A4})$$

with learnable weights $W_{k'}^{(t)}$ or those of $\text{NN}^{(t)}$ initialized by picking the respective entries from a normal distribution with zero mean and unit variance. Linear readout functions for $t < T$ preserve the many-body orders in $\mathbf{h}_{uk(L=0)}^{(t)}$, while a one-layer fully-connected NN is used for the last message-passing layer and accounts for the residual higher-order terms in the expansion [32].

B.3 Asymptotic computational complexity

We analyze the computational complexity of the irreducible Cartesian tensor product with respect to the maximum rank L used. For each tuple of (i_1, \dots, i_L) of a rank- L tensor in Eq. (2), the single contraction term $(\mathbf{x}_L \cdot (k+m) \cdot \mathbf{y}_L)$ has a computational complexity of $\mathcal{O}(3^{k+m})$. The total computational complexity is $\mathcal{O}(3^L)$ for even products and $\mathcal{O}(3^{L+1})$ for odd ones—due to the additional double contraction with the Levi-Civita symbol. The computation of the set of permutations over the L unsymmetrized indices scales as $L!/(2^{L/2}(L/2)!)$ for even products and $L!/(2^{(L-1)/2}((L-1)/2)!)$ for odd ones [45]. Because each final rank- L tensor has 3^L elements, the total complexity for computing an irreducible Cartesian tensor of rank L is $\mathcal{O}(9^L L!/(2^{L/2}(L/2)!))$.

Recent state-of-the-art equivariant message-passing architectures employ tensors of rank $L \leq 4$ [32, 33, 78]. Also, physical properties are represented by tensors of rank $L \leq 4$. For these spherical tensors, the number of calculations required to obtain an element of a new L -rank tensor is $(2L+1)^5$, or $(2L+1)^6$ for a $(2L+1)$ -dimensional object \mathbf{Y}^L . Thus, the irreducible Cartesian tensor product is expected to be more computationally efficient for $L \leq 4$, assuming similar multiplicative factors and negligible sub-leading terms. Compared to the Gaunt tensor product with $(2L+1)^3$, irreducible Cartesian tensors are expected to be less computationally efficient for $L \geq 3$. However, while the Gaunt tensor product is restricted only to even parity, i.e., it excludes tensors with odd $l_1 + l_2 - l_3 = 2k+1$ (e.g., pseudo-vectors), the irreducible Cartesian tensor product naturally allows their computation.

As regards the cost of performing message passing at each layer, the general neighbors' aggregation of Eq. (4) has a cost of $\mathcal{O}(\mathcal{E} 9^L L!/(2^{L/2}(L/2)!))$, where \mathcal{E} is the number of edges in the system. Similarly, computing the many-body features tensor via Eq. (6) requires to perform ν Cartesian tensor products for all $\mathcal{K} = \text{len}(\eta_\nu)$ possible ν -fold tensor products, resulting in an asymptotic complexity of $\mathcal{O}(\mathcal{MK}\nu 9^L L!/(2^{L/2}(L/2)!))$ with \mathcal{M} denoting the number of nodes. Thus, the computational complexity for one ICTP message-passing layer is $\mathcal{O}((\mathcal{E} + \mathcal{MK}\nu) 9^L L!/(2^{L/2}(L/2)!))$.

Finally, memory consumption for Cartesian tensors is often believed to be less advantageous than that of spherical tensors. However, for contracting two rank- L spherical tensors, space complexity is about $(2L+1)^2$, resulting from the definition of the Clebsch–Gordan tensor product in Section 2, i.e., due to the computation of intermediate tensors $\mathbf{Y}^L \otimes \mathbf{Y}^L \in \mathbb{R}^{(2L+1) \times (2L+1)}$. For a Cartesian tensor, the space complexity is about 3^L . Thus, the irreducible Cartesian tensor product can be expected to require the same or less memory for $L \leq 4$ than the Clebsch–Gordan counterpart.

C Proof of Cartesian message-passing equivariance to actions of the orthogonal group

We first recap the standard action of the $O(3)$ group onto $(\mathbb{R}^3)^{\otimes l}$. Let $D_{\mathcal{X}}$ be a representation of the orthogonal group $O(3)$ (also in line with Section 2), i.e.,

$$D_{\mathcal{X}} : O(3) \rightarrow \mathbb{R}^{3 \times 3}, \quad g \mapsto D_{\mathcal{X}}[g] = R.$$

We define the action of the $O(3)$ group onto $(\mathbb{R}^3)^{\otimes l}$ as follows

$$\phi : O(3) \times (\mathbb{R}^3)^{\otimes l} \rightarrow (\mathbb{R}^3)^{\otimes l}, \quad \phi(g, \mathbf{T}_l)_{i_1 i_2 \dots i_l} := \sum_{j_1} \dots \sum_{j_l} R_{i_1 j_1} \dots R_{i_l j_l} (\mathbf{T}_l)_{j_1 \dots j_l},$$

where $\mathbf{T}_l \in (\mathbb{R}^3)^{\otimes l}$. We hereinafter denote $\phi(g, \mathbf{T}_l)$ also by $R\mathbf{T}_l$. The outer product \otimes is equivariant to this action, and R acts trivially on the 3×3 -identity matrix.

Lemma C.1. *Let R be a representation of an element of the orthogonal group $O(3)$. Then,*

- (i) $\forall \mathbf{T}_{l_1} \in (\mathbb{R}^3)^{\otimes l_1}$ and $\forall \mathbf{T}_{l_2} \in (\mathbb{R}^3)^{\otimes l_2}$

$$R(\mathbf{T}_{l_1} \otimes \mathbf{T}_{l_2}) = (R\mathbf{T}_{l_1}) \otimes (R\mathbf{T}_{l_2}).$$
- (ii) *For the 3×3 -identity matrix \mathbf{I} , we have*

$$R\mathbf{I} = \mathbf{I}.$$

Proof. (i) We first show that $R(\mathbf{T}_{l_1} \otimes \mathbf{T}_{l_2}) = (R\mathbf{T}_{l_1}) \otimes (R\mathbf{T}_{l_2})$

$$\begin{aligned} & ((R\mathbf{T}_{l_1}) \otimes (R\mathbf{T}_{l_2}))_{i_1 \dots i_{l_1} i_{l_1+1} \dots i_{l_1+l_2}} = \\ & (R\mathbf{T}_{l_1})_{i_1 \dots i_{l_1}} (R\mathbf{T}_{l_2})_{i_{l_1+1} \dots i_{l_1+l_2}} = \\ & \left(\sum_{j_1} \dots \sum_{j_{l_1}} R_{i_1 j_1} \dots R_{i_{l_1} j_{l_1}} (\mathbf{T}_{l_1})_{j_1 \dots j_{l_1}} \right) \left(\sum_{j_{l_1+1}} \dots \sum_{j_{l_1+l_2}} R_{i_{l_1+1} j_{l_1+1}} \dots R_{i_{l_1+l_2} j_{l_1+l_2}} (\mathbf{T}_{l_2})_{j_{l_1+1} \dots j_{l_1+l_2}} \right) = \\ & \sum_{j_1} \dots \sum_{j_{l_1}} \sum_{j_{l_1+1}} \dots \sum_{j_{l_1+l_2}} R_{i_1 j_1} \dots R_{i_{l_1} j_{l_1}} R_{i_{l_1+1} j_{l_1+1}} \dots R_{i_{l_1+l_2} j_{l_1+l_2}} (\mathbf{T}_{l_1})_{j_1 \dots j_{l_1}} (\mathbf{T}_{l_2})_{j_{l_1+1} \dots j_{l_1+l_2}} \\ & = (R(\mathbf{T}_{l_1} \otimes \mathbf{T}_{l_2}))_{i_1 \dots i_{l_1} i_{l_1+1} \dots i_{l_1+l_2}}. \end{aligned}$$

(ii) With $\sum_i R_{ij} R_{ik} = \delta_{jk}$, or equivalently $R^T R = \mathbf{I}$, we get

$$(R\mathbf{I})_{i_1 i_2} = \sum_{j_1, j_2} R_{i_1 j_1} R_{i_2 j_2} \delta_{j_1 j_2} = \sum_{j_1} R_{i_1 j_1} R_{i_2 j_1} = \delta_{i_1 i_2}.$$

□

Using Lemma C.1, we can show that the irreducible Cartesian tensor operator $\mathbf{T}_l : \mathbb{R}^3 \rightarrow (\mathbb{R}^3)^{\otimes l}$ is equivariant to actions of the $O(3)$ group.

Proposition C.2. *Let $l \geq 0$ be a positive integer. Then, the irreducible Cartesian tensor operator $\mathbf{T}_l : \mathbb{R}^3 \rightarrow (\mathbb{R}^3)^{\otimes l}$ is equivariant to actions of the $O(3)$ group.*

Proof. It suffices to show that the map $\hat{\mathbf{r}} \mapsto \hat{\mathbf{r}}^{\otimes(l-2m)} \otimes \mathbf{I}^{\otimes m}$ is equivariant to actions of the $O(3)$ group $\forall l \geq 1$ and $\forall m \leq \lfloor l/2 \rfloor$ ($m \geq 0$).

$$\begin{aligned} (R\hat{\mathbf{r}})^{\otimes(l-2m)} \otimes \mathbf{I}^{\otimes m} & \stackrel{\text{Lemma C.1 (ii)}}{=} (R\hat{\mathbf{r}})^{\otimes(l-2m)} \otimes (R\mathbf{I})^{\otimes m} \\ & \stackrel{\text{Lemma C.1 (i)}}{=} R \left(\hat{\mathbf{r}}^{\otimes(l-2m)} \otimes \mathbf{I}^{\otimes m} \right). \end{aligned}$$

□

Our next claim is that for $l_3 \in \{|l_1 - l_2|, |l_1 - l_2| + 1, \dots, l_1 + l_2\}$ the irreducible Cartesian tensor product \otimes_{Cart} defined in Eqs. (2) and (3) is equivariant to actions of the $O(3)$ group, i.e., the following diagram commutes

$$\begin{array}{ccc} (\mathbb{R}^3)^{\otimes l_1} \times (\mathbb{R}^3)^{\otimes l_2} & \xrightarrow{\otimes_{\text{Cart}}} & (\mathbb{R}^3)^{\otimes l_3} \\ R \downarrow & & \downarrow R \\ (\mathbb{R}^3)^{\otimes l_1} \times (\mathbb{R}^3)^{\otimes l_2} & \xrightarrow{\otimes_{\text{Cart}}} & (\mathbb{R}^3)^{\otimes l_3} \end{array}$$

The proof for this claim is very similar to Proposition C.2. The only difference is to show the equivariance for the $(k + m)$ -fold tensor contraction.

Proposition C.3. *The irreducible Cartesian tensor product $\otimes_{\text{Cart}} : (\mathbb{R}^3)^{\otimes l_1} \times (\mathbb{R}^3)^{\otimes l_2} \rightarrow (\mathbb{R}^3)^{\otimes l_3}$ makes the above diagram commute.*

Proof. It suffices to show that the $(k + m)$ -fold tensor contraction is equivariant to actions of the $O(3)$ group. For $\mathbf{x}_{l_1} \in (\mathbb{R}^3)^{\otimes l_1}$, $\mathbf{y}_{l_2} \in (\mathbb{R}^3)^{\otimes l_2}$, and R being a representation of an element of the orthogonal group $O(3)$, we can write

$$\begin{aligned} & ((R\mathbf{x}_{l_1}) \cdot (s) \cdot (R\mathbf{y}_{l_2}))_{\beta_1 \dots \beta_{l_1-s} \delta_1 \dots \delta_{l_2-s}} = \\ & \sum_{\alpha_1, \dots, \alpha_s} (R\mathbf{x}_{l_1})_{\alpha_1 \dots \alpha_s \beta_1 \dots \beta_{l_1-s}} (R\mathbf{y}_{l_2})_{\alpha_1 \dots \alpha_s \delta_1 \dots \delta_{l_2-s}} = \\ & \sum_{\alpha_1, \dots, \alpha_s} \left(\sum_{\substack{\gamma_1, \dots, \gamma_s \\ \eta_1, \dots, \eta_{l_1-s}}} R_{\alpha_1 \gamma_1} \dots R_{\alpha_s \gamma_s} R_{\beta_1 \eta_1} \dots R_{\beta_{l_1-s} \eta_{l_1-s}} (\mathbf{x}_{l_1})_{\gamma_1 \dots \gamma_s \eta_1 \dots \eta_{l_1-s}} \right) \times \\ & \left(\sum_{\substack{\tilde{\gamma}_1, \dots, \tilde{\gamma}_s \\ \tilde{\eta}_1, \dots, \tilde{\eta}_{l_2-s}}} R_{\alpha_1 \tilde{\gamma}_1} \dots R_{\alpha_s \tilde{\gamma}_s} R_{\delta_1 \tilde{\eta}_1} \dots R_{\delta_{l_2-s} \tilde{\eta}_{l_2-s}} (\mathbf{y}_{l_2})_{\tilde{\gamma}_1 \dots \tilde{\gamma}_s \tilde{\eta}_1 \dots \tilde{\eta}_{l_2-s}} \right) = \\ & \left(\sum_{\tilde{\eta}_1 \dots \tilde{\eta}_{l_1-s}} R_{\beta_1 \eta_1} \dots R_{\beta_{l_1-s} \eta_{l_1-s}} \right) \left(\sum_{\tilde{\eta}_1 \dots \tilde{\eta}_{l_2-s}} R_{\delta_1 \tilde{\eta}_1} \dots R_{\delta_{l_2-s} \tilde{\eta}_{l_2-s}} \right) \times \\ & \sum_{\gamma_1 \dots \gamma_s} (\mathbf{x}_{l_1})_{\gamma_1 \dots \gamma_s \eta_1 \dots \eta_{l_1-s}} (\mathbf{y}_{l_2})_{\gamma_1 \dots \gamma_s \tilde{\eta}_1 \dots \tilde{\eta}_{l_2-s}} = \\ & (R(\mathbf{x}_{l_1} \cdot (s) \cdot \mathbf{y}_{l_2}))_{\beta_1 \dots \beta_{l_1-s} \delta_1 \dots \delta_{l_2-s}}. \end{aligned}$$

A similar derivation applies to the odd case (3), which completes the proof. \square

We finally give a proof for Proposition 4.1, i.e., the equivariance of message-passing layers based on irreducible Cartesian tensors to actions of the $O(3)$ group.

Proof of Proposition 4.1. Since a message-passing layer in Section 4.2 and Appendix B.2 is defined by stacking layers corresponding to Eqs. (4), (5), (6), (A1), (A2), and (A3), we show the equivariance for each of these equations. We show the equivariance by induction.

• Case $t = 1$:

Equivariance of Eq. (5): Since learnable weights W_{kZ_v} and learnable (invariant) radial basis $R_{kl_1}^{(1)}(r_{uv})$ are defined for each feature channel k , the weights are multiplied with $(\mathbf{T}_{l_1}(\hat{\mathbf{r}}_{uv}))_{i_1 i_2 \dots i_{l_1}}$ as scalars. Therefore,

$$(\mathbf{A}_{ukl_1}^{(1)})_{i_1 i_2 \dots i_{l_1}} = \sum_{v \in \mathcal{N}(u)} R_{kl_1}^{(1)}(r_{uv}) (\mathbf{T}_{l_1}(\hat{\mathbf{r}}_{uv}))_{i_1 i_2 \dots i_{l_1}} W_{kZ_v}$$

is equivariant to actions of the $O(3)$ group.

Equivariance of Eq. (6): The proof is similar to the case of Eq. (5), since we again have learnable parameter $W_{kk'l_\nu}^{(1)}$ for each $\mathbf{A}_{uk'l_\nu}^{(1)}$. Therefore, noting that the Cartesian tensor product is equivariant to actions of the $O(3)$ group, the following function

$$(\mathbf{B}_{u\eta_\nu kL}^{(1)})_{i_1 i_2 \dots i_L} = (\tilde{\mathbf{A}}_{ukl_1}^{(1)} \otimes_{\text{Cart}} \dots \otimes_{\text{Cart}} \tilde{\mathbf{A}}_{ukl_\nu}^{(1)})_{i_1 i_2 \dots i_L}$$

is also equivariant to actions of the $O(3)$ group.

Equivariance of Eq. (A1): The equation defined by

$$(\mathbf{m}_{ukL}^{(1)})_{i_1 i_2 \dots i_L} = \left(\sum_{\nu} \sum_{\eta_\nu} W_{Z_u \eta_\nu kL}^{(1)} \mathbf{B}_{u\eta_\nu kL}^{(1)} \right)_{i_1 i_2 \dots i_L},$$

is equivariant to actions of the $O(3)$ group, since for each set of indices u, η_ν, k , and L we have a scalar learnable parameter $W_{Z_u \eta_\nu kL}^{(1)}$.

Equivariance of Eq. (A2): The respective parameters $W_{kk'L}^{(1)}$ and $W_{Z_u kk'L}^{(1)}$ in Eq. (A2)

$$(\mathbf{h}_{ukL}^{(2)})_{i_1 i_2 \dots i_L} = \frac{1}{\sqrt{d_t}} \sum_{k'} W_{kk'L}^{(1)} (\mathbf{m}_{uk'L}^{(1)})_{i_1 i_2 \dots i_L} + \frac{1}{\sqrt{d_t N_Z}} \sum_{k'} W_{Z_u kk'L}^{(1)} (\mathbf{h}_{uk'L}^{(1)})_{i_1 i_2 \dots i_L}.$$

are multiplied as scalar with $\mathbf{h}_{uk'L}^{(1)}$ and $\mathbf{m}_{uk'L}^{(1)}$, which are shown to be equivariant to actions of the $O(3)$ group. Thus, $\mathbf{h}_{ukL}^{(2)}$ is equivariant to actions of the $O(3)$ group as a function of $\mathbf{h}_{uk'L}^{(1)}$ and $\mathbf{m}_{uk'L}^{(1)}$.

Equivariance of Eq. (A3): The equivariance of Eq. (A3) to actions of the $O(3)$ group is also immediate since learnable parameters apply to each tuple of (i_1, i_2, \dots, i_L) as a scalar.

- General case $t > 1$: The equivariance of Eqs. (4), (5), (6), (A1), (A2), and (A3) to actions of the $O(3)$ group for arbitrary $t > 1$ follows in a similar way to those obtained for the $t = 1$ case. However, we need to show the equivariance of Eq. (4). Suppose that Eqs. (5), (6), (A1), (A2), and (A3) are equivariant to actions of the $O(3)$ group for $t > 1$. Then, for the $(t+1)$ -th message-passing layer,

$$(\mathbf{A}_{ukl_3}^{(t)})_{i_1 i_2 \dots i_{l_3}} = \sum_{v \in \mathcal{N}(u)} \left(R_{kl_1 l_2 l_3}^{(t)}(r_{uv}) \mathbf{T}_{l_1}(\hat{\mathbf{r}}_{uv}) \otimes_{\text{Cart}} \frac{1}{\sqrt{d_t}} \sum_{k'} W_{kk'l_2}^{(t)} \mathbf{h}_{vk'l_2}^{(t)} \right)_{i_1 i_2 \dots i_{l_3}},$$

is equivariant to actions of the $O(3)$ group. Here, the irreducible Cartesian tensor product \otimes_{Cart} and \mathbf{T}_{l_1} are equivariant to actions of the $O(3)$ group, $\mathbf{h}_{vk'l_2}^{(t)}$ is equivariant by the assumption, and $W_{kk'l_2}^{(t)}$ applies to $\mathbf{h}_{vk'l_2}^{(t)}$ as a scalar.

□

D Experiments and results

D.1 Description of the data sets

rMD17 data set. The revised MD17 (rMD17) data set is a collection of structures, energies, and atomic forces of ten small organic molecules obtained from ab initio molecular dynamics (AIMD) [47]. These molecules are derived from the original MD17 data set [47, 80–82], with 100,000 structures sampled for each. Our models are trained using 950 and 50 configurations for each molecule randomly sampled from the original data set using five random seeds, with 50 additional configurations randomly sampled for early stopping. We use the remaining configurations to test the final models. Table 1 reports the mean absolute errors (MAEs) in total energies and atomic forces averaged over five independent runs, including the standard deviation between them.

3BPA data set. The 3BPA data set comprises structures, energies, and atomic forces of a flexible drug-like organic molecule obtained from AIMD at various temperatures [48]. The training data set consists of 500 configurations sampled at 300 K, while three separate test data sets are obtained from AIMD simulations at 300 K, 600 K, and 1200 K. An additional test data set provides energy values

along dihedral rotations of the molecule. This test directly assesses the smoothness and accuracy of the potential energy surface, influencing properties such as binding free energies to protein targets. Our models are trained using 450 and 50 configurations randomly sampled from the training data set using five random seeds, with further 50 configurations reserved for early stopping. Table 2 reports the root-mean-square errors (RMSEs) in total energies and atomic forces averaged over five independent runs, including the standard deviation between them.

Acetylacetone data set. The acetylacetone data set includes structures, energies, and atomic forces of a small reactive molecule obtained from AIMD at various temperatures [32]. The training data set comprises configurations sampled at 300 K, while the test data sets are sampled at 300 K and 600 K. The generalization ability of final models is evaluated using an elevated temperature of 600 K and along two internal coordinates of the molecule: The hydrogen transfer path and a partially conjugated double bond rotation featuring a high rotation barrier. Our models are trained using 450 and 50 configurations randomly sampled from the training dataset using five random seeds, with further 50 configurations reserved for early stopping. Table 3 reports the root-mean-square errors (RMSEs) in total energies and atomic forces averaged over five independent runs, including the standard deviation between them.

D.2 Training details

All ICTP and MACE models employed in this work are trained on a single NVIDIA A100 GPU with 80 GB of RAM. Training times for ICTP and MACE models are typically between 30 minutes and 15 hours, depending on the data set, the data set size, and the employed precision. We use double precision for 3BPA and AcAc data sets and single precision for rMD17, in line with the original experiments [33]. For all experiments, we use two message-passing layers and irreducible Cartesian tensors or spherical tensors of a maximal rank of $l_{\max} = 3$ to embed the directional information of atomic distance vectors. For ICTP models with the full and symmetric product basis (ICTP_{full} and ICTP_{sym}, respectively) and MACE, we employ 256 uncoupled feature channels. For ICTP models with the symmetric product basis evaluated in the latent feature space (ICTP_{sym+lt}), we use 64 coupled feature channels for the Cartesian product basis and 256 for two-body features. Radial features are derived from eight Bessel basis functions with polynomial envelope for the cutoff with $p = 5$ [70]. These features are fed into a fully connected NN of size [64, 64, 64]. We apply SiLU non-linearities to the outputs of the hidden layers [83, 84]. The readout function of the first message-passing layer is implemented as a linear layer. The readout function of the second layer is a single-layer fully connected NN with 16 hidden neurons. A cutoff radius of 5 Å is used across all data sets.

All parameters of ICTP and MACE models are optimized by minimizing the combined squared loss on training data $\mathcal{D}_{\text{train}} = (\mathcal{X}_{\text{train}}, \mathcal{Y}_{\text{train}})$, where $\mathcal{X}_{\text{train}} = \{\mathcal{S}^{(k)}\}_{k=1}^{N_{\text{train}}}$ and $\mathcal{Y}_{\text{train}} = \{E_k^{\text{ref}}, \{\mathbf{F}_{u,k}^{\text{ref}}\}_{u=1}^{N_{\text{at}}}\}_{k=1}^{N_{\text{train}}}$:

$$\mathcal{L}(\theta, \mathcal{D}_{\text{train}}) = \sum_{k=1}^{N_{\text{train}}} \left[C_e \left\| E_k^{\text{ref}} - E(\mathcal{S}^{(k)}, \theta) \right\|_2^2 + C_f \sum_{u=1}^{N_{\text{at}}} \left\| \mathbf{F}_{u,k}^{\text{ref}} - \mathbf{F}_u(\mathcal{S}^{(k)}, \theta) \right\|_2^2 \right]. \quad (\text{A5})$$

When training ICTP models, we set $C_e = 1/N_{\text{at}}^{(k)}$ and $C_f = 10 \text{ Å}^2$ to balance the relative contributions of total energies and atomic forces, respectively. For MACE, $C_e = 1/(B \times N_{\text{at}}^{(k)})$ and $C_f = 1000/(B \times 3 \times N_{\text{at}}^{(k)}) \text{ Å}^2$ are used with B denoting the batch size. Here, $E(\mathcal{S}^{(k)}, \theta)$ and $\mathbf{F}_u(\mathcal{S}^{(k)}, \theta)$ are total energies and atomic forces predicted by ICTP or MACE.

All models are trained for 2000 epochs using the AMSGrad variant of Adam [85], with default parameters of $\beta_1 = 0.9$, $\beta_2 = 0.999$, and $\varepsilon = 10^{-8}$. We use a learning rate of 0.01 and a batch size of 5 for all experiments. For evaluations on the validation and test data sets, we use a batch size of 10. The learning rate is reduced using an on-plateau scheduler based on the validation loss with a patience of 50 and a decay factor of 0.8. We utilize an exponential moving average with a weight of 0.99 for evaluation on the validation set and for the final model. Additionally, in line with MACE [33], we apply exponential weight decay of 5×10^{-7} on the weights of Eqs. (6), (A1), and (A3). Furthermore, we incorporate a per-atom shift of total energies via the average per-atom energy over all the training configurations, including the energies of individual atoms for 3BPA and acetylacetone datasets. If no atomic energies are provided, as for rMD17, the per-atom shift is obtained by solving a linear

Table A1: **Energy (E) and force (F) root-mean-square errors (RMSEs) for the 3BPA data set.** E- and F-RMSE are provided in meV and meV/Å, respectively. Results are presented for models trained using 50 molecules randomly drawn from the training data set collected at 300 K, while additional 50 are used for early stopping. All values for ICTP and MACE models are obtained by averaging over five independent runs, with the standard deviation provided if available. Best performances, considering the standard deviation, are highlighted in bold.

		ICTP _{full}	ICTP _{sym}	ICTP _{sym+lt}	MACE
300 K	E	14.98 ± 1.62	13.43 ± 1.00	16.03 ± 1.26	14.54 ± 1.02
	F	37.21 ± 2.14	37.27 ± 1.63	38.38 ± 1.55	37.68 ± 1.33
600 K	E	31.68 ± 3.56	31.63 ± 3.94	30.74 ± 1.82	30.71 ± 3.43
	F	69.87 ± 3.04	68.87 ± 2.94	69.62 ± 2.88	69.88 ± 3.88
1200 K	E	92.16 ± 9.33	86.0 ± 12.03	78.51 ± 8.88	83.99 ± 8.20
	F	157.72 ± 6.53	153.16 ± 9.62	151.37 ± 9.59	154.46 ± 10.84
Dihedral slices	E	33.69 ± 8.03	31.06 ± 6.27	33.44 ± 5.56	27.79 ± 7.41
	F	47.12 ± 5.27	47.68 ± 2.21	49.08 ± 4.05	48.91 ± 4.71

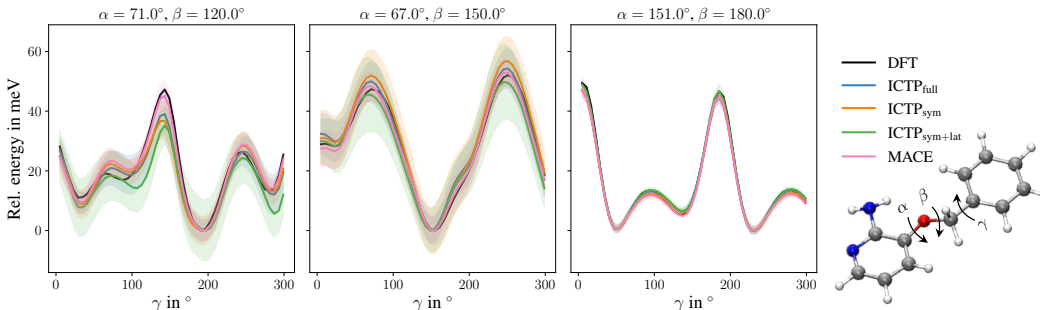


Figure A1: **Potential energy profiles for three cuts through the 3BPA molecule’s potential energy surface.** All models are trained using 450 configurations, and the remaining 50 are used for early stopping. The 3BPA molecule, including the three dihedral angles (α , β , and γ), provided in degrees $^\circ$, is shown as an inset. The color code of the inset molecule is C grey, O red, N blue, and H white. The reference potential energy profile (DFT) is shown in black. Each profile is shifted such that each model’s lowest energy is zero. Shaded areas denote standard deviations across five independent runs.

regression problem [56]. Additionally, a per-atom scale is determined as the root-mean-square of the components of the forces over the training configurations.

D.3 Additional results

Extrapolation to out-of-domain data. Table A1 demonstrates total energy and atomic force RMSEs obtained for ICTP and MACE models trained using 50 configurations randomly drawn from the original data set. ICTP and MACE models perform similarly, considering the standard deviation obtained across five independent runs. However, ICTP models often have lower mean RMSE values compared to MACE.

Figure A1 compares potential energy profiles obtained with ICTP and MACE models trained using 450 configurations. Potential energy cuts at $\beta = 120^\circ$ and $\beta = 180^\circ$ are easier tasks for MLIPs, as there are training points in the data set with similar combinations of dihedral angles [32]. In contrast, the potential energy cut at $\beta = 150^\circ$ is more challenging, with no training points close to it. Notably, Fig. A1 shows that all models produce smooth potential energy profiles close to the reference ones (DFT) for all values of β . These results again demonstrate excellent extrapolation capabilities of irreducible Cartesian models that are on par with the spherical MACE model.

Table A2: **Energy (E) and force (F) root-mean-square errors (RMSEs) for the acetylacetone data set.** E- and F-RMSE are provided in meV and meV/Å, respectively. Results are presented for models trained using 50 configurations randomly drawn from the training data set collected at 300 K, while additional 50 are used for early stopping. All values for ICTP and MACE models are obtained by averaging over five independent runs. Best performances, considering the standard deviation, are highlighted in bold.

		ICTP _{full}	ICTP _{sym}	ICTP _{sym+lt}	MACE
300 K	E	4.42 ± 0.39	4.45 ± 0.36	4.38 ± 0.24	4.22 ± 0.52
	F	28.85 ± 3.00	28.28 ± 1.45	29.17 ± 1.65	28.38 ± 2.74
600 K	E	17.61 ± 3.14	16.13 ± 1.37	17.3 ± 2.05	17.53 ± 3.58
	F	75.09 ± 8.70	69.99 ± 5.12	74.96 ± 4.68	74.93 ± 9.91

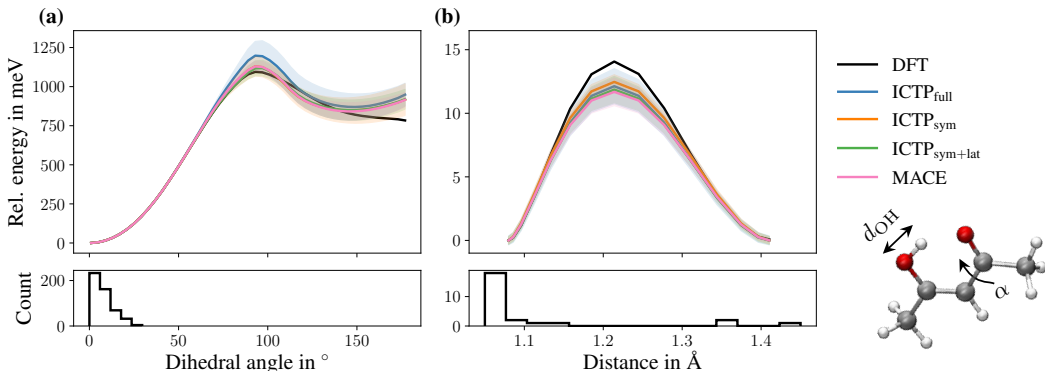


Figure A2: **Potential energy profiles of (a) the dihedral angle describing the rotation around the C-C bond and (b) hydrogen transfer between two oxygen atoms.** All models are trained using 450 molecules, and the remaining 50 are used for early stopping. The acetylacetone molecule, including the dihedral angle in degrees $^{\circ}$ describing the rotation around the C-C bond (α), is shown as an inset in (a). The color code of the inset molecule is C grey, O red, and H white. The reference potential energy profile (DFT) is shown in black. Each profile is shifted such that each model’s lowest energy is zero. The histograms demonstrate the distribution of dihedral angles and O-H distances in the training data. Shaded areas denote standard deviations across five independent runs.

Flexibility and reactivity. Table A2 demonstrates total energy and atomic force RMSEs obtained for ICTP and MACE models trained using 50 configurations randomly drawn from the original data set. Similar to the 3BPA data set, ICTP and MACE models demonstrate comparable accuracy in predicted energies and forces, considering the standard deviation obtained across five independent runs.

Figure A2 further investigates the generalization capabilities of ICTP models trained using 450 configurations, demonstrating potential energy profiles for the rotation around the C-C bond, i.e., the C-C-C-O dihedral angle (α), and for the hydrogen transfer. The training data set encompasses dihedral angles less than 30° . Furthermore, the energy barrier of 1 eV is outside the energy range of the training data set obtained at 300 K. As for the hydrogen transfer, the training data does not contain transition geometries, but the reaction still occurs in a region that is not too far from the training data. Overall, ICTP models perform on par with MACE for predicting potential energy profiles for the rotation around the corresponding C-C bond and for the hydrogen transfer.

Figure A3 shows potential energy profiles for MLIPs trained with 50 configurations, similar to Fig. A2. Notably, Fig. A2 (b) demonstrates that ICTP_{full} is the only MLIP consistently producing the potential energy profile for the hydrogen transfer close to the reference (DFT). This task is particularly challenging, as most data splits do not include configurations sufficiently close to the transition structure as in Fig. A2.

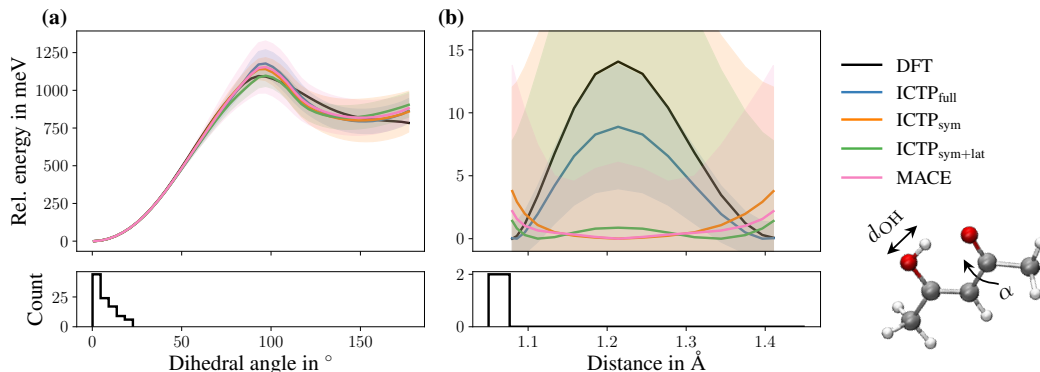


Figure A3: **Potential energy profiles of (a) the dihedral angle describing the rotation around the C-C bond and (b) hydrogen transfer between two oxygen atoms.** All models are trained using 50 molecules, and additional 50 are used for early stopping. The acetylacetone molecule, including the dihedral angle in degrees $^{\circ}$ describing the rotation around the C-C bond (α), is shown as an inset in (a). The color code of the inset molecule is C grey, O red, and H white. The reference potential energy profile (DFT) is shown in black. Each profile is shifted such that each model's lowest energy is zero. The histograms demonstrate the distribution of dihedral angles and O-H distances in the training data set for one random seed used to split the original data. Shaded areas denote standard deviations across five independent runs.

E Broader social impact

This section discusses the broader social impact of the presented work. Our work has important implications for the chemical sciences and engineering, as many problems in these fields require atomistic simulations; we also discuss it in Section 1. Although this work focuses on standard benchmark data sets, our experiments demonstrate the scalability of our method to larger atomic systems. Beyond constructing machine-learned interatomic potentials, equivariant models based on irreducible Cartesian tensors can be applied for molecular property prediction, protein structure prediction, protein generation, RNA structure ranking, and many more.

Our work has no obvious negative social impact. As long as it is applied to the chemical sciences and engineering in a way that benefits society, it will have positive effects.